Volume complexity of dS bubbles

Roberto Auzzi,[1,2,*] Giuseppe Nardelli,[1,3,†] Gabriel Pedde Ungureanu,[4,‡] and Nicolò Zenoni[5,§]

[1]*Dipartimento di Matematica e Fisica, Università Cattolica del Sacro Cuore, Via della Garzetta 48, 25133 Brescia, Italy*

[2]*INFN Sezione di Perugia, Via A. Pascoli, 06123 Perugia, Italy*

[3]*TIFPA—INFN, c/o Dipartimento di Fisica, Università di Trento, 38123 Povo (TN), Italy*

[4]*SISSA, Via Bonomea 265, 34136 Trieste, Italy*

[5]*Department of Physics, Osaka University, Toyonaka, Osaka 560-0043, Japan*

(Received 7 April 2023; accepted 21 June 2023; published 10 July 2023)

In the framework of the static patch approach to de Sitter holography introduced in [L. Susskind, J. Hologr. Appl. Phys. **1**, 1 (2021)], the growth of holographic complexity has a hyperfast behavior, which leads to a divergence in a finite time. This is very different from the anti–de Sitter (AdS) spacetime, where instead the complexity rate asymptotically reaches a constant value. We study holographic volume complexity in a class of asymptotically AdS geometries which include de Sitter bubbles in their interior. With the exception of the static bubble case, the complexity obtained from the volume of the smooth extremal surfaces which are anchored just to the AdS boundary has a similar behavior to the AdS case, because it asymptotically grows linearly with time. The static bubble configuration has a zero complexity rate and corresponds to a discontinuous behavior, which resembles a first order phase transition. If instead we consider extremal surfaces which are anchored at both the AdS boundary and the de Sitter stretched horizon, we find that complexity growth is hyperfast, as in the de Sitter case.

DOI: 10.1103/PhysRevD.108.026006

I. INTRODUCTION

The AdS/CFT correspondence [1] provides an interesting theoretical laboratory to address many important open questions in quantum gravity. However, our observed universe is rather different from an AdS background. It is then a crucial problem to find a quantum gravity formulation for a cosmological setting. It is interesting to investigate generalizations of holography for de Sitter (dS) spacetime. This is a challenging problem, because in dS there is no natural notion of timelike boundary contrary to asymptotically AdS spacetime.

In order to provide a holographic description of dS, the dS/CFT correspondence [2–4] proposes a duality between quantum gravity in dS_D spacetime and a $(D-1)$-dimensional CFT living on a spacelike boundary at the future spacelike infinity in dS. Examples of explicit dS/CFT correspondence have been proposed for higher spin gravity in four dimensions [5] and for 3-dimensional Einstein gravity [6,7]. The boundary theory in these cases is not unitary and rather exotic compared to the textbook examples of CFTs, because it describes dS from the perspective of a metaobserver who lives at the future infinity.

A finite entropy can be associated with the area A of the dS cosmological horizon [8] surrounding a static patch observer. Following [9–11], if we consider a dS spacetime which includes particles and black holes, we can define a generalized entropy $S_{\rm gen}$ which includes the cosmological horizon entropy and the ordinary entropy $S_{\rm out}$ of the matter which can be seen by the observer at the center of the static patch

$$S_{\rm gen} = \frac{A}{4G} + S_{\rm out}, \tag{1.1}$$

where we denote by G the Newton constant. It has been argued that the maximum possible value of $S_{\rm gen}$ is saturated by the empty dS spacetime [9,10,12]. The presence of a bound for $S_{\rm gen}$ motivates another class of approaches to holography for dS space, see for example [13–18], in which gravity in dS is conjectured to be dual to a quantum mechanical system with a finite number of degrees of freedom.

Quantum information provides a useful conceptual framework to implement several entries of the dictionary

*roberto.auzzi@unicatt.it
†giuseppe.nardelli@unicatt.it
‡gpeddeun@sissa.it
§nicolo@hetmail.phys.sci.osaka-u.ac.jp

of holographic dualities, and might give precious insights on how to formulate holography for the dS spacetime [19–21]. An interesting generalization of the Ryu-Takayanagi [22,23] entanglement entropy formula has been proposed in the context of static patch horizon holography in dS [24–26]. In this proposal, the AdS boundary is replaced in dS by a stretched horizon which is taken just inside the cosmological horizon that surrounds a static patch observer. The Bekenstein-Hawking entropy associated to the cosmological horizon [8] is then interpreted as the entanglement entropy between the left and right static patches. Further recent works include [27–33].

Computational complexity is another concept in quantum information theory which may play an important role in holography, see [34–36] for reviews. Indeed, entanglement entropy saturates too fast to describe the growth of the Einstein-Rosen bridge inside a black hole horizon [37] in terms of the boundary CFT. On the other hand, quantum complexity saturates in a much larger timescale compared to the thermalization one, so it has the correct behavior [34,38] to overcome the limitations of entanglement entropy. In theoretical computer science, complexity [39] measures how hard it is to build a generic target state from a simple reference one, applying a set of elementary gates. For quantum systems with a finite number of degrees of freedom, a continuous notion of complexity was introduced by Nielsen [40] in terms of the length of geodesics in the space of unitary operators. There is a large amount of arbitrariness in the definition of complexity, due to the choice of reference state and of the computational cost of elementary gates. Despite these ambiguities, quantum complexity is expected to exhibit several robust and universal properties [41], provided that the computational costs of elementary gates is chosen in such a way that the complexity metric has negative curvature [42–47]. It is still an open problem to generalize Nielsen's approach to complexity in quantum field theory. Many advances have been made in defining complexity in free field theory [48,49]. The definition of complexity in CFT is still a work in progress, see [50–54].

Three main proposals have been extensively studied as a holographic dual of quantum computational complexity:

(i) Complexity=volume (CV) [55], in which complexity is proportional to the volume of the maximal codimension-one spatial surface anchored at a boundary time slice.
(ii) Complexity=action (CA) [56,57], in which complexity is proportional to the gravitational action evaluated on a codimension-zero bulk region, called the Wheeler-DeWitt patch.
(iii) Complexity=volume 2.0, in which complexity is proportional to the spacetime volume of the Wheeler-DeWitt patch [58].

Further generalizations have been investigated in [59–61]. All these holographic proposals reproduce the expected behavior of quantum complexity for an AdS black hole: in the regime of bulk classical gravity, which should be appropriate for times which are less than exponential in the entropy of the system [62], complexity asymptotically grows linearly with time.

As studied in [24,63], the definition of holographic complexity can be extended to static patch horizon holography in dS [24–26]. Much differently compared to AdS, holographic complexity in dS exhibits a hyperfast growth, i.e., the complexity growth is so fast that it diverges at a finite critical time. In [24], Susskind proposed the hyperfast growth to be a signature that the Hamiltonian of the dual of dS is not of the usual k-local type. Here k-local means that the Hamiltonian is the sum of terms that simultaneously act at most on k degrees of freedom, where k is parametrically of order unity in the limit of a large number of degrees of freedom.

It is tempting to relate the hyperfast growth of complexity in dS to the exponential growth of spacetime. In order to further investigate the reason of a different time dependence of holographic complexity compared to AdS, it is interesting to contemplate intermediate situations. At the crossroad between AdS and dS holography, we can consider gravity backgrounds with an asymptotically AdS_D boundary which include dS_D regions in their interior. Examples in $D = 2$ include the centaur geometry [64,65], which can be built in dilaton-gravity theories.[1] For centaurs, the dS part of the spacetime is not hidden behind an AdS black hole horizon. Holographic volume complexity in these backgrounds was recently studied in [67]. In this case, the evolution of complexity is qualitatively different compared to both AdS and dS cases, because complexity is a decreasing function of time.

In this paper, we study volume complexity in higher-dimensional examples of asymptotically AdS spacetimes with dS bubbles in their interior [68,69]. This kind of geometries can be realized, for instance, in an Einstein-scalar theory where the potential has various minima separated by a domain wall. The $D \geq 3$ case significantly differs from the $D = 2$ one, since in higher dimensions the dS portion of the geometry is always screened by an AdS horizon at late time. In order to simplify the model, it is useful to consider the limit in which the thickness of the domain wall surrounding the dS interior is small compared to the other physical scales, as studied in [70–72] for a flat external space and in [68,69] for an AdS external region. For simplicity, we specialize to $D = 3$ bulk spacetime dimensions and we consider spherically symmetric geometries consisting of a dS region and an asymptotically AdS spacetime separated by a domain wall with negligible thickness. We set the AdS scale to one, and we parametrize the dS cosmological constant by λ and the domain wall tension by κ. Outside the bubble, the solution is a BTZ

[1]Related studies of dS bubbles in dilaton gravity include [66].

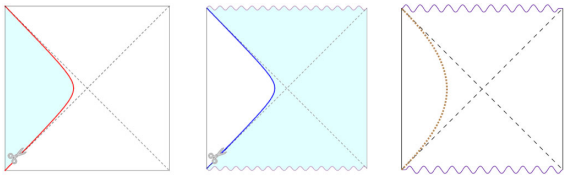

FIG. 1. Penrose diagrams for a static bubble. We show in red and in blue the bubble trajectory in dS (left) and in AdS (center), respectively. Our geometry (on the right) is obtained by joining the dS portion to the left of the red line with the AdS region to the right of the blue line.

black hole [73] with mass proportional to μ. While the parameters λ and κ specify the theory, μ is a property of the state.

We focus on backgrounds which are invariant under time-reversal symmetry $t \to -t$. For the critical value $\mu = \mu_0$, where

$$\mu_0 = \frac{\sqrt{(\kappa^2+\lambda-1)^2+4\lambda}-(\kappa^2+\lambda-1)}{2\lambda}, \quad (1.2)$$

the only time-reversal invariant solution is the static bubble, see Fig. 1. For $\mu > \mu_0$, the bubble starts from zero radius and expands to infinite size, without entering the external true vacuum region. From the viewpoint of an external observer, the bubble remains behind a black hole horizon. However, no such bubble solution exists which enjoys time-reversal invariance. So, in this paper we focus on the regime $\mu \leq \mu_0$.

For a fixed $\mu < \mu_0$, there are two time-reversal invariant solutions:

(i) A bubble collapsing in a finite proper time, for which the interior portion of dS has finite spacetime volume. We refer to this case as "small bubble" solution. We have to further distinguish between two subcases. For $0 < \mu < \mu_s$, where

$$\mu_s = \frac{1}{\kappa^2+\lambda} < \mu_0, \quad (1.3)$$

the dS bubble is initially on the same side of the Penrose diagram as the AdS boundary. We refer to this configuration as a "very small bubble," see Fig. 2. For $\mu_s < \mu < \mu_0$ the bubble is initially on the opposite side of the Penrose diagram with respect to the AdS boundary. We call this situation a "not so small bubble," see Fig. 3.

(ii) A bubble expanding for an infinite proper time, which contains an infinite portion of the dS spacetime. We refer to this case as "large bubble" solution. We here introduce

$$\mu_h = \frac{1-\kappa^2}{\lambda} < \mu_0. \quad (1.4)$$

For $0 < \mu < \mu_h$, the interior of the bubble contains as a subset a dS static patch. We call this situation a "very large bubble," see Fig. 4. By contrast, we refer to the solution with $\mu_h < \mu < \mu_0$ as a "not so large bubble," see Fig. 5. Note that very large bubbles can only be obtained for small enough domain wall tension, i.e., $\kappa < 1$.

In the parameter space, the static bubble configuration is at the border between the small and the large bubble regimes.

With the exception of the very small bubble, in all cases an observer outside the horizon cannot directly see the dS bubble at any time, because it is screened by the black hole horizon. The presence of the dS bubble is instead detected by the volume complexity, because the extremal surface always penetrates the dS region of the geometry.

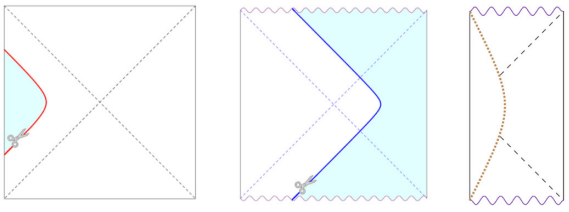

FIG. 2. Penrose diagrams for a very small bubble $0 < \mu < \mu_s$.

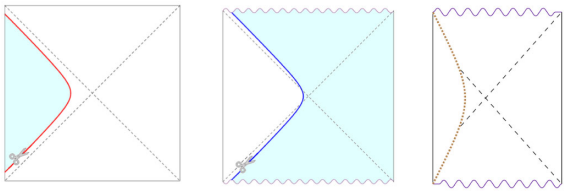

FIG. 3. Penrose diagrams for a not so small bubble $\mu_s < \mu < \mu_0$.

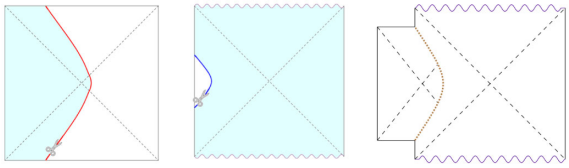

FIG. 4. Penrose diagrams for a very large bubble $0 < \mu < \mu_h$ (top panel) and for a not so large bubble $\mu_h < \mu < \mu_0$ (lower panel).

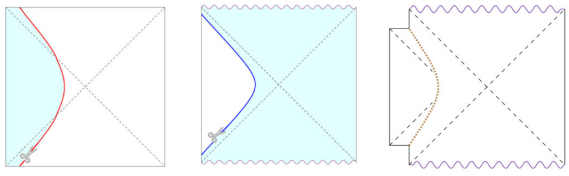

FIG. 5. Penrose diagrams for a not so large bubble $\mu_h < \mu < \mu_0$.

The traditional way to apply the CV proposal is to consider the volume of extremal surfaces which are anchored at the AdS boundary and which are smooth both in the AdS and in the dS portions of the spacetime. This prescription can be applied both for large and small bubbles. With the exception of the static bubble configuration, we find that at late time holographic complexity grows linearly with the same slope as for the BTZ black hole. In the fine-tuned case of the static bubble, we find instead that volume complexity is time-independent.

The time dependence of complexity that we obtain reveals that the hyperfast growth is not necessarily related to the exponential growth of spacetime, which is a feature of large bubbles. If we consider the prescription in which smooth extremal surfaces are anchored just at the AdS boundary, we find that the dS portion of the extremal surface always remains in the dS static patches, without entering the regions behind the dS horizon. This is the reason why the exponential growth of large bubbles fails to be detected by volume complexity.

As proposed in [68], the boundary dual of a large bubble configuration should be a a quantum field theory in a mixed state. This observation can be justified as follows. For time-reversal symmetric bubbles, Eq. (1.2) implies that

$$\lambda\mu \leq \lambda\mu_0 \leq 1, \tag{1.5}$$

which is equivalent to

$$S_{\rm BH} \leq S_{\rm dS}, \tag{1.6}$$

where $S_{\rm BH}$ is the entropy of the external AdS black hole and $S_{\rm dS}$ is the entropy of the internal dS static patch $S_{\rm dS}$, i.e.,

$$S_{\rm BH} = 2\pi\sqrt{\mu}, \qquad S_{\rm dS} = \frac{2\pi}{\sqrt{\lambda}}. \tag{1.7}$$

For large bubbles, the interior region contains a portion of the dS horizon, so the number of degrees of freedom accessible from the AdS boundary is less than the number of degrees of freedom of the internal dS region. We are then forced to interpret large bubbles configurations in AdS/CFT as gravity duals of a density matrix, obtained by tracing over a part of the degrees of freedom of the dS region inside the bubble.

In the context of static patch horizon holography in dS [24–26], we can conjecture that the purification of the dual mixed state is a generalization of thermofield double state [74] in which the CFT living at the boundary of AdS and the quantum system living on the stretched dS horizon are entangled. This suggests another way to apply the CV proposal in the case of very large bubbles: we can anchor extremal surfaces both at the AdS boundary and at the dS static patch stretched horizon. In this case, we find that extremal surfaces cross the dS horizon and tend to bend toward the future infinity. The complexity growth is hyperfast and diverges in finite time, as in the dS case.

The paper is organized as follows. In Sec. II we describe the bubble setup and the thin wall approximation. In Sec. III we present the equations of the extremal surfaces both in AdS and in dS and we discuss the refraction law for the extremal surface on the bubble. In Sec. IV we study volume complexity, using the prescription in which the extremal surfaces are anchored just at the AdS boundary and are smooth both in the AdS and in the dS regions of the spacetime. In Sec. V we study volume complexity for very large bubbles, using extremal surfaces which extend between the AdS boundary and the dS stretched horizon. We conclude in Sec. VI. Several technical details are presented in appendices.

II. THEORETICAL SETUP

We consider a spherically symmetric dS_3 bubble inside an asymptotically AdS_3 spacetime. The spacetime metric is taken as follows

$$\begin{aligned} ds^2_{i,o} &= (g_{i,o})_{\mu\nu} dx^\mu_{i,o} dx^\nu_{i,o} \\ &= -f_{i,o}(r) dt^2_{i,o} + \frac{dr^2}{f_{i,o}(r)} + r^2 d\theta^2, \end{aligned} \tag{2.1}$$

where the subscripts i and o refer to the inside and outside regions, respectively. The outside geometry is a BTZ black hole [73] with

$$f_o(r) = r^2 - \mu, \tag{2.2}$$

where the mass of the black hole is proportional to μ. For simplicity we set the AdS length $L = 1$. The inside geometry is a dS_3 spacetime with radius $r_{dS} = 1/\sqrt{\lambda}$, namely

$$f_i(r) = 1 - \lambda r^2. \tag{2.3}$$

Introducing the tortoise coordinate

$$r^*_{i,o} = \int \frac{d\tilde{r}}{f_{i,o}(\tilde{r})}, \tag{2.4}$$

we can define the light-cone coordinates v, u as follows

$$v_{i,o} = t_{i,o} + r^*_{i,o}(r), \qquad u_{i,o} = t_{i,o} - r^*_{i,o}(r). \tag{2.5}$$

An explicit evaluation of the integral (2.4) gives

$$\begin{aligned} r^*_o(r) &= \frac{1}{4\sqrt{\mu}} \log\left(\frac{r-\sqrt{\mu}}{r+\sqrt{\mu}}\right)^2, \\ r^*_i(r) &= \frac{1}{4\sqrt{\lambda}} \log\left(\frac{1+r\sqrt{\lambda}}{1-r\sqrt{\lambda}}\right)^2, \end{aligned} \tag{2.6}$$

where the integration constants are chosen in such a way that $r_o^*(\infty) = 0$ and $r_i^*(0) = 0$.

When considering spacetime regions nearby the black hole and the cosmological horizons, it is convenient to write the metric in Eddington-Finkelstein (EF) coordinates $(v_{i,o}, r)$ or $(u_{i,o}, r)$:

$$\begin{aligned} ds_{i,o}^2 &= -f_{i,o}(r)dv_{i,o}^2 + 2drdv_{i,o} + r^2 d\theta^2 \\ &= -f_{i,o}(r)du_{i,o}^2 - 2drdu_{i,o} + r^2 d\theta^2. \end{aligned} \tag{2.7}$$

In order to describe the maximally extended versions of the dS_3 and the BTZ spacetimes, it is necessary to introduce two copies of the EF coordinates u and v, which we denote by u_L, v_L and u_R, v_R, where L and R stand for left and right, respectively. Penrose diagrams for these geometries with constant u, v lines are shown in Fig. 6. Our conventions for Penrose diagrams are discussed in Appendix A.

A. The domain wall

The inside and the outside geometries are patched together along a domain wall with negligible thickness, whose trajectory on each side of the spacetime is parametrized by

$$r = R(\tau), \tag{2.8}$$

with τ the proper time measured on the domain wall itself. We will denote by a dot $\cdot$ the derivative with respect to the proper time τ.

The equation of motion for $R(\tau)$ follows from Israel's junction conditions [75] (see [68–70,76] for reviews), i.e.:

(i) The metric must be continuous across the wall. The coordinate r multiplies the metric of the transverse sphere S^1, so it is continuous. Instead, the coordinate $t_{i,o}$ is in general discontinuous in passing from inside to outside.

(ii) The discontinuity in the extrinsic curvature K_{ab} across the wall is fixed by the energy-momentum tensor. For spherically symmetric geometries, it is customary to introduce the quantities

$$\beta_{i,o} = (K_\theta^\theta)_{i,o} R. \tag{2.9}$$

The jump between β_i and β_o is

$$\beta_i - \beta_o = \kappa R, \tag{2.10}$$

where in our case

$$\begin{aligned} \beta_i &= \pm\sqrt{\dot{R}^2 + f_i(R)}, \\ \beta_o &= \pm\sqrt{\dot{R}^2 + f_o(R)}, \\ \kappa &= 8\pi G\sigma. \end{aligned} \tag{2.11}$$

In Eq. (2.11), σ is the domain wall tension and G is the Newton's constant. The sign of $\beta_{i,o}$ is positive if the coordinate r increases as the wall is approached from the interior or as one moves away from the wall in the exterior, and negative in the opposite situations. If both $\beta_{i,o}$ have the same sign, r is monotonic near the wall. If $\beta_{i,o}$ have different signs, r is locally extremized at the location of the wall.

Squaring twice Eq. (2.10), independently of the choices of signs in Eq. (2.11), the equation of motion can be expressed as

$$\dot{R}^2 + V(R) = 0, \tag{2.12}$$

where the second term, playing the role of an effective potential, is

$$V(R) = f_o(R) - \frac{(f_i(R) - f_o(R) - \kappa^2 R^2)^2}{4\kappa^2 R^2}. \tag{2.13}$$

Specializing the general expression (2.13) to Eqs. (2.3) and (2.2), we find

$$V(R) = -AR^2 + B - \frac{C}{R^2}, \tag{2.14}$$

where

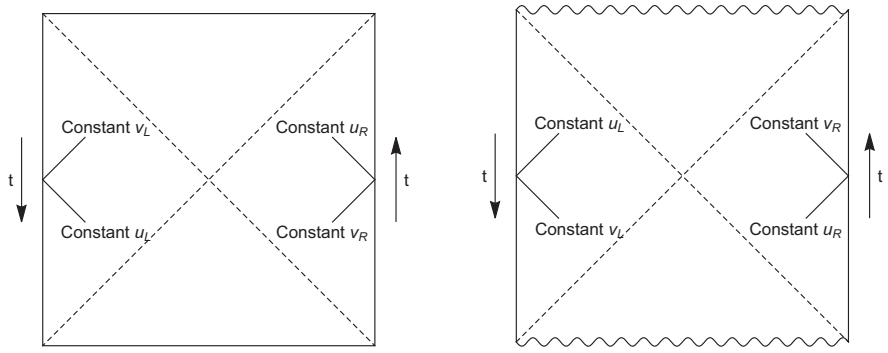

FIG. 6. Penrose diagrams for dS_3 spacetime (left) and for the BTZ black hole (right). The arrows show the directions of increasing coordinate t on both the sides of the diagrams.

$$A = \frac{(\lambda+\kappa^2-1)^2+4\lambda}{4\kappa^2},$$
$$B = \frac{1+\kappa^2+\lambda+\mu-\kappa^2\mu+\lambda\mu}{2\kappa^2},$$
$$C = \frac{(1+\mu)^2}{4\kappa^2}. \tag{2.15}$$

Note that $A > 0$ and $C > 0$. It is also convenient to introduce

$$\beta = \frac{B}{A}, \qquad \gamma = \frac{C}{A}. \tag{2.16}$$

Depending on the values of parameters, we can have three physically different situations:

(i) The maximum of $V(R)$ is positive. In this case, the radius of the bubble as a function of the bubble proper time τ has either a maximum or a minimum.
(ii) The maximum of $V(R)$ is exactly zero. In this case, we have an unstable static bubble solution, besides other solutions which approach the maximum from both sides with asymptotically zero velocity $\dot{R}$.
(iii) The maximum of $V(R)$ is negative. In this case, the radius of the bubble monotonically contracts or expands without any maximum or minimum.

The qualitative behavior of $V(R)$ in these three cases is shown in Fig. 7.

Time-reversal invariance selects a potential $V(R)$ with non-negative maximum, as in cases (a) and (b). This requires

$$\beta^2 \geq 4\gamma. \tag{2.17}$$

For time-reversal symmetric bubbles, an explicit integration of Eq. (2.12) gives

$$R(\tau) = \sqrt{\frac{\beta}{2} \mp \frac{\sqrt{\beta^2-4\gamma}}{2}\cosh(2\sqrt{A}\tau)}. \tag{2.18}$$

The—sign solution corresponds to a small bubble (the bubble has maximal radius at $\tau = 0$ and collapses in a finite proper time), whereas the + sign solution describes a large bubble (the bubble has minimal radius at $\tau = 0$ and expands forever).

The condition in Eq. (2.17) is is satisfied for $0 < \mu \leq \mu_0$, where the limiting value $\mu = \mu_0$ is defined in Eq. (1.2) and corresponds to a static bubble.

For a given choice of the parameters λ, μ, κ with $\mu < \mu_0$ it is possible to have both a contracting and an expanding solution. The maximal radius for the contracting bubble is

$$R_{\max}(\mu) = \sqrt{\frac{\beta}{2} - \frac{\sqrt{\beta^2-4\gamma}}{2}}, \tag{2.19}$$

while the minimal radius for the expanding bubble is

$$R_{\min}(\mu) = \sqrt{\frac{\beta}{2} + \frac{\sqrt{\beta^2-4\gamma}}{2}}. \tag{2.20}$$

Both $R_{\max}$ and $R_{\min}$ are real positive numbers for $0 < \mu \leq \mu_0$. The values of $R_{\max}$ and $R_{\min}$ satisfy the following constraints:

(i) $R_{\max} \leq R_{\min}$, with the equality saturated for $\mu = \mu_0$.
(ii) $R_{\min} \leq 1/\sqrt{\lambda}$, with the equality saturated for the special value $\mu = \mu_h$, see Eq. (1.4).
(iii) $R_{\max} \geq \sqrt{\mu}$ with the equality saturated for the special value $\mu = \mu_s$, see Eq. (1.3).

In Fig. 8 we show a plot of $R_{\max}$ and $R_{\min}$ as functions of μ, for a fixed value of λ and κ.

In order to specify the solution, we should also determine the time coordinates $t_{i,o}$ on the surface of the bubble, both in the inside and in the outside regions. Such time coordinates, which we denote by $T_{i,o}(\tau)$, are specified by the equation

$$\dot{T}^2_{i,o} = \frac{1}{f_{i,o}(R)}\left(1 + \frac{\dot{R}^2}{f_{i,o}(R)}\right), \tag{2.21}$$

following from the normalization of the bubble velocity vector w^α

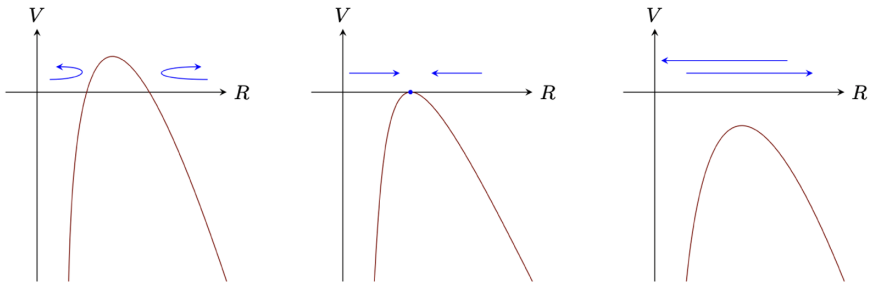

(a) (b) (c)

FIG. 7. Qualitative plots of the effective potential $V(R)$ in Eq. (2.14) with positive (plot a), vanishing (plot b) and negative (plot c) maximum. Blue arrows represent the possible evolution of the bubble radius $R(\tau)$.

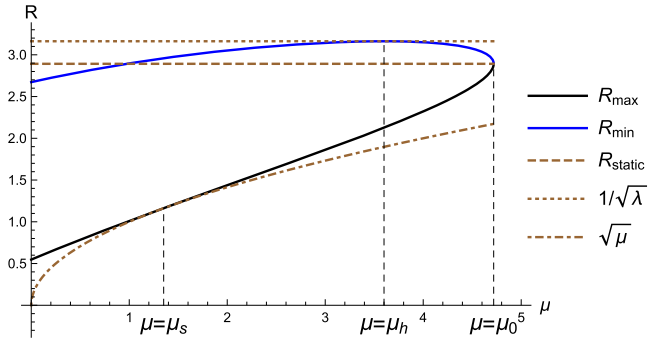

FIG. 8. Illustrative plot of $R_{\max}$ and $R_{\min}$ as functions of μ, for $\lambda = 0.1$ and $\kappa = 0.8$.

$$w^\alpha w_\alpha = -1, \qquad w^\alpha = (\dot{T}, \dot{R}, 0). \tag{2.22}$$

Combining the equation of motion (2.12) with Eq. (2.21) we find

$$\frac{dT_{i,o}}{dR} = \pm \frac{\sqrt{f_{i,o}(R) - V(R)}}{f_{i,o}(R)\sqrt{-V(R)}}. \tag{2.23}$$

Plugging the explicit expressions for f_i and f_o in Eq. (2.23), we get

$$\begin{aligned} \frac{dT_i}{dR} &= \pm \frac{1}{2\kappa} \frac{1 + \mu - R^2(1 + \lambda - \kappa^2)}{(1 - \lambda R^2)\sqrt{AR^4 - BR^2 + C}}, \\ \frac{dT_o}{dR} &= \pm \frac{1}{2\kappa} \frac{1 + \mu - R^2(1 + \lambda + \kappa^2)}{(R^2 - \mu)\sqrt{AR^4 - BR^2 + C}}. \end{aligned} \tag{2.24}$$

Time-reversal solutions to these equations are obtained by imposing the boundary condition

$$T_{i,o}(R_{\max}) = 0 \quad \text{or} \quad T_{i,o}(R_{\min}) = 0 \tag{2.25}$$

in the collapsing and the expanding case, respectively.

B. Static bubbles

A static bubble solution is realized for $\beta^2 = 4\gamma$, or equivalently $\mu = \mu_0$, see Eq. (1.2). The radius of the bubble is thus

$$R_{\text{static}} = R_{\min}(\mu_0) = R_{\max}(\mu_0). \tag{2.26}$$

The matching condition between the $T_{i,o}$ coordinates is

$$\frac{dT_i}{dT_o} = \pm \sqrt{\frac{f_o(R_{\text{static}})}{f_i(R_{\text{static}})}} = \pm \mu_0. \tag{2.27}$$

C. Small bubbles

In this case, Eq. (2.24) admits a smooth solution for T_i. On the other hand, the trajectory is not smooth in the coordinate T_o, which should then be replaced by an EF coordinate, see Eq. (2.5). Referring to the Penrose diagrams for the collapsing bubble sketched in Figs. 2 and 3, we distinguish between two cases:

(i) Very small bubble, $0 < \mu < \mu_s$. The initial position of the bubble $R = R_{\max}$ is on the same side of the AdS boundary. The smooth coordinates that should be used are v_{R} for the black hole (or u_{R} for the white hole). Denoting by $U_{\text{R},o}$ and $V_{\text{R},o}$ the right EF coordinates on the bubble surface in BTZ spacetime, the equations of motion are

$$\begin{aligned} \frac{dV_{\text{R},o}}{dR} &= -\frac{1}{2\kappa} \frac{1 + \mu - R^2(1 + \lambda + \kappa^2)}{(R^2 - \mu)\sqrt{AR^4 - BR^2 + C}} + \frac{1}{R^2 - \mu}, \\ \frac{dU_{\text{R},o}}{dR} &= \frac{1}{2\kappa} \frac{1 + \mu - R^2(1 + \lambda + \kappa^2)}{(R^2 - \mu)\sqrt{AR^4 - BR^2 + C}} - \frac{1}{R^2 - \mu}. \end{aligned} \tag{2.28}$$

(ii) Not so small bubble, $\mu_s < \mu < \mu_0$. In this case we should use u_{L} for the black hole (or v_{L} for the white hole). Denoting by $U_{\text{L},o}$ and $V_{\text{L},o}$ the left EF coordinates on the bubble surface in BTZ spacetime, the equations of motion are

$$\begin{aligned} \frac{dU_{\text{L},o}}{dR} &= -\frac{1}{2\kappa} \frac{1 + \mu - R^2(1 + \lambda + \kappa^2)}{(R^2 - \mu)\sqrt{AR^4 - BR^2 + C}} - \frac{1}{R^2 - \mu}, \\ \frac{dV_{\text{L},o}}{dR} &= \frac{1}{2\kappa} \frac{1 + \mu - R^2(1 + \lambda + \kappa^2)}{(R^2 - \mu)\sqrt{AR^4 - BR^2 + C}} + \frac{1}{R^2 - \mu}. \end{aligned} \tag{2.29}$$

D. Large bubbles

Large bubbles are examples of bags of gold [69,77], which are defined as spacetimes in which an eternal black hole exterior is attached by an Einstein-Rosen bridge to an interior which is a portion of Friedman-Lemaitre-Robertson-Walker (FLRW) cosmology with an infinite spacetime volume. In these geometries, the entropy of the interior can exceed the exterior Bekenstein-Hawking entropy, see Eq. (1.6), so the bulk states cannot be put in correspondence with the CFT states of the dual field theory. It has been suggested that the Bekenstein-Hawking entropy does not in general count all the states inside the black hole, but only those which are distinguishable from the outside [77,78]. In particular, large bubble solutions has been proposed to provide the holographic dual of a density matrix [68].

Equation (2.24) for the outside time T_o gives a smooth solution, while T_i is singular because the dS horizon is

crossed at some time by the bubble. We then pass to EF coordinates, see Eq. (2.5). With reference to the Penrose diagrams for the expanding bubble sketched in Figs. 4 and 5, we discriminate between two cases:

(i) Very large bubble, $0 < \mu < \mu_h$. The initial position of the bubble $R = R_{\min}$ is in the right static patch. Denoting by $U_{\mathrm{R},i}$ and $V_{\mathrm{R},i}$ the right EF coordinates on the bubble surface in dS, the equations of motion are

$$\frac{dV_{\mathrm{R},i}}{dR} = \frac{1}{2\kappa}\frac{1+\mu-R^2(1+\lambda-\kappa^2)}{(1-\lambda R^2)\sqrt{AR^4-BR^2+C}} + \frac{1}{1-\lambda R^2},$$
$$\frac{dU_{\mathrm{R},i}}{dR} = -\frac{1}{2\kappa}\frac{1+\mu-R^2(1+\lambda-\kappa^2)}{(1-\lambda R^2)\sqrt{AR^4-BR^2+C}} - \frac{1}{1-\lambda R^2}. \tag{2.30}$$

(ii) Not so large bubble, $\mu_h < \mu < \mu_0$. The initial position of the bubble $R = R_{\min}$ is in the left static patch. Denoting by $U_{\mathrm{L},i}$ and $V_{\mathrm{L},i}$ the left EF coordinates on the bubble surface in dS, the equations of motion are

$$\frac{dU_{\mathrm{L},i}}{dR} = \frac{1}{2\kappa}\frac{1+\mu-R^2(1+\lambda-\kappa^2)}{(1-\lambda R^2)\sqrt{AR^4-BR^2+C}} - \frac{1}{1-\lambda R^2},$$
$$\frac{dV_{\mathrm{L},i}}{dR} = -\frac{1}{2\kappa}\frac{1+\mu-R^2(1+\lambda-\kappa^2)}{(1-\lambda R^2)\sqrt{AR^4-BR^2+C}} + \frac{1}{1-\lambda R^2}. \tag{2.31}$$

III. VOLUME FUNCTIONAL

According to the CV conjecture [55], complexity of the boundary state is proportional to the volume of a maximal codimension-one surface anchored at the given boundary time. The volume complexity C_V is usually normalized as

$$C_V = \frac{\mathcal{V}}{GL}, \tag{3.1}$$

where $\mathcal{V}$ is the volume of the maximal slice, G the Newton's constant and L the AdS radius. In this section we discuss the volume of extremal surfaces in both the AdS and the dS parts of the geometry. Then, we address the matching condition on the domain wall.

Due to spherical symmetry, the extremal surface can be parametrized as

$$r = r(l), \qquad t = t(l), \tag{3.2}$$

where l is a single-valued coordinate along the surface. Since the coordinate t is singular nearby the horizons, it is useful to write the volume functional in both the versions of the EF coordinates u and v:

$$\mathcal{V}_{i,o} = 2\pi\int \mathcal{L}dl,$$
$$\mathcal{L} = r\sqrt{-f_{i,o}(v'_{i,o})^2 + 2r'v'_{i,o}}$$
$$= r\sqrt{-f_{i,o}(u'_{i,o})^2 - 2r'u'_{i,o}}, \tag{3.3}$$

where $'$ denotes a derivative with respect to l. The extremal surface is characterized by a conserved quantity $P_{i,o}$, which in the (v,r) and in the (u,r) coordinates reads

$$P_{i,o} = \frac{\partial\mathcal{L}}{\partial v'_{i,o}} = \frac{r(-f_{i,o}v'_{i,o}+r')}{\sqrt{-f_{i,o}(v'_{i,o})^2+2r'v'_{i,o}}},$$
$$P_{i,o} = \frac{\partial\mathcal{L}}{\partial u'_{i,o}} = \frac{r(-f_{i,o}u'_{i,o}-r')}{\sqrt{-f_{i,o}(u'_{i,o})^2-2r'u'_{i,o}}}, \tag{3.4}$$

respectively.

The volume functional in Eq. (3.3) is invariant under reparametrization in l. To fix this gauge freedom, it is convenient to impose the conditions

$$\sqrt{-f_{i,o}(v'_{i,o})^2+2r'v'_{i,o}} = r \quad \text{or}$$
$$\sqrt{-f_{i,o}(u'_{i,o})^2-2r'u'_{i,o}} = r, \tag{3.5}$$

in such a way that the volume functional becomes

$$\mathcal{V}_{i,o} = 2\pi\int r^2 dl. \tag{3.6}$$

With this gauge choice, the conserved quantity $P_{i,o}$ can be expressed as follows

$$P_{i,o} = -f_{i,o}v'_{i,o} + r', \qquad v'_{i,o} = \frac{r'-P_{i,o}}{f_{i,o}},$$
$$P_{i,o} = -f_{i,o}u'_{i,o} - r', \qquad u'_{i,o} = \frac{-r'-P_{i,o}}{f_{i,o}}. \tag{3.7}$$

By inserting this back into the gauge constraint, we get

$$(r')^2 + U_{i,o}(r) = P_{i,o}^2, \qquad U_{i,o}(r) = -f_{i,o}(r)r^2,$$
$$r' = \pm\sqrt{P_{i,o}^2 + f_{i,o}(r)r^2}, \tag{3.8}$$

which is valid in both the EF coordinate systems (v,r) and (u,r). The conserved quantity $P_{i,o}$ can also be written as

$$P_{i,o} = -f_{i,o}t'_{i,o}. \tag{3.9}$$

Note that $U_{i,o}(r)$ in Eq. (3.8) can be interpreted as effective potentials, see Fig. 9 for qualitative plots.

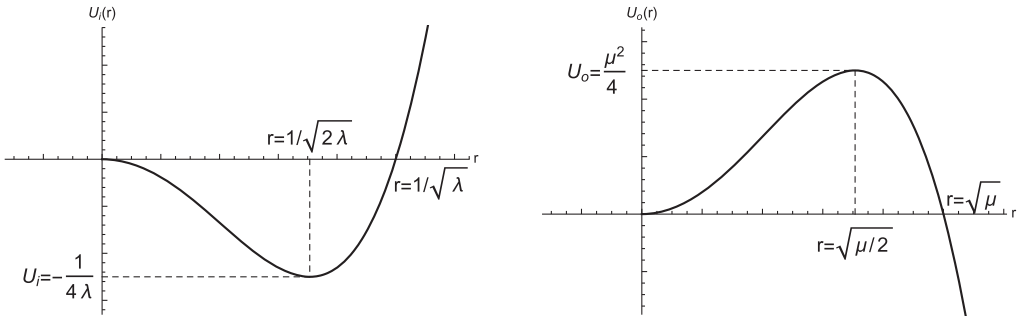

FIG. 9. Effective potential for the extremal surface in the dS region (left) and in the AdS one (right).

The extremum of $r(l)$ represents a turning point r_t for the extremal surface. We can have a turning point both in the external BTZ region and in the internal dS one:

(i) In the external asymptotically AdS region, $r_{t,\mathrm{AdS}}$ is a minimum of $r(l)$, given by

$$r_{t,\mathrm{AdS}} = \sqrt{\frac{\mu + \sqrt{\mu^2 - 4P_o^2}}{2}}. \tag{3.10}$$

For a turning point to exist, it is necessary to require

$$P_o^2 \leq P_{\max}^2 = \frac{\mu^2}{4}. \tag{3.11}$$

(ii) In the internal dS region, $r_{t,\mathrm{dS}}$ is a maximum of $r(l)$, given by

$$r_{t,\mathrm{dS}} = \sqrt{\frac{1 + \sqrt{1 + 4\lambda P_i^2}}{2\lambda}}. \tag{3.12}$$

The difference in the time coordinate t between two points on the extremal surface can be expressed as

$$t_{i,o}(r_2) - t_{i,o}(r_1) = \mp \int_{r_1}^{r_2} \frac{P_{i,o}}{f_{i,o}\sqrt{P_{i,o}^2 + f_{i,o}(r) r^2}} dr, \tag{3.13}$$

where the $-$ sign should be chosen for a parametrization with $r'(l) > 0$, while the $+$ sign for a parametrization with $r'(l) < 0$. In the integral in Eq. (3.13), the Cauchy principal value prescription should be used when crossing the horizon.

With the convention $r_2 > r_1$, the volume of the extremal surface reads

$$\mathcal{V}_{i,o} = 2\pi \int_{r_1}^{r_2} \frac{r^2}{\sqrt{P_{i,o}^2 + f_{i,o}(r) r^2}} dr. \tag{3.14}$$

A. A refraction law for the extremal surface

To determine the codimension-one extremal surfaces, we solve Eqs. (3.8) and (3.7) both in the interior and in the exterior of the bubble. Then, we match the two solutions on top of the domain wall, imposing that the total volume is extremal. Physically, the extremal surface is somehow "refracted" by the domain wall. In Appendix B, by introducing a coordinate system which describes both the interior and the exterior of the bubble in terms of the same time coordinate t_i, we derive the refraction condition in the thin wall approximation.

By spherical symmetry, it is not restrictive to focus just on the time and radial coordinates. We denote by $x_{i,o}^\mu(l)$ the coordinates of the extremal codimension-one surface and by $X_{i,o}^\mu(\tau)$ the trajectory of the domain wall. We then introduce the tangent vector to the extremal surface $\frac{dx_{i,o}^\mu}{dl}$ and the velocity vector of the domain wall $\frac{dX_{i,o}^\mu}{d\tau}$, namely

$$\begin{aligned} \frac{dx_{i,o}^\mu}{dl} &= (t'_{i,o}(l), r'_{i,o}(l)), \\ \frac{dX_{i,o}^\mu}{d\tau} &= (\dot{T}_{i,o}(\tau), \dot{R}(\tau)). \end{aligned} \tag{3.15}$$

The matching condition on top of the domain wall is

$$(g_i)_{\mu\nu} \frac{dx_i^\mu}{dl} \frac{dX_i^\nu}{d\tau} = (g_o)_{\mu\nu} \frac{dx_o^\mu}{dl} \frac{dX_o^\nu}{d\tau}. \tag{3.16}$$

The details of the derivation are in Appendix B. A similar result was derived in [79] for geodesics.

Given an extremal surface intersecting the domain wall at some value of the radial coordinate R, we denote by $\rho_{i,o}(R)$ the value of $r'_{i,o}(l)$ computed at the intersection, i.e.,

$$\rho_{i,o}(R) = r'_{i,o}(l_0) \quad \text{where } r_{i,o}(l_0) = R. \tag{3.17}$$

By means of Eq. (3.9), we can write the matching condition (3.16) as

$$P_i \frac{dT_i}{dR} + \frac{\rho_i(R)}{f_i(R)} = P_o \frac{dT_o}{dR} + \frac{\rho_o(R)}{f_o(R)}. \tag{3.18}$$

The setup with an extremal surface crossing a null shell of matter with negligible thickness was studied in [80] for geodesics and in [81,82] for codimension-one surfaces. This case formally corresponds to a domain wall moving at the speed of light and the result is consistent with Eq. (3.18).

IV. COMPLEXITY FROM SMOOTH EXTREMAL SURFACES

The conservative way to apply the CV conjecture in asymptotically AdS geometries with an internal dS bubble is to consider extremal codimension one surfaces which are anchored at some given time t_b at the AdS boundary and which are smooth in the interior. These surfaces lie partially in the dS and partially in the asymptotically AdS parts of the geometry. By convention, we choose l in Eq. (3.2) to be positive and to vanish at the center of the dS static patch.

In order to avoid a singularity at $r = 0$ in the dS interior, we must impose the condition $P_i = 0$. This can be checked as follows. Using Eqs. (3.9) and (3.8), the induced metric on the extremal surface in the gauge (3.5) is

$$d\tilde{s}_i^2 = r^2(l)(dl^2 + d\theta^2). \tag{4.1}$$

From Eq. (3.8), $r(l)$ can have two qualitatively different behaviors nearby $l \to 0$:

(i) For $P_i = 0$, $r(l) \approx r'(l)$, so the induced metric

$$d\tilde{s}_i^2 \approx dr^2 + r^2 d\theta^2$$

is smooth at $l \to 0$, with $0 \le \theta \le 2\pi$.

(ii) For $P_i \neq 0$, $r^2(l) \approx P_i^2 l^2$, so the induced metric

$$d\tilde{s}_i^2 \approx P_i^2(l^2 dl^2 + l^2 d\theta^2)$$

has a singular scalar curvature at $l \to 0$.

A similar property holds in the case of AdS Vaidya spacetime, see [81].

Equation (3.9) implies that for $P_i = 0$ the extremal surface in the interior lies at constant t_i coordinate. Examples of these surface are shown in Fig. 10.

A. Small bubbles

For small bubbles, the inside geometry is just a region of the left static patch. Then, there is no turning point in the dS portion of the geometry, or equivalently $r_i'(l) > 0$. As a direct consequence, we have $\rho_i(R) > 0$ everywhere on the domain wall. With the condition $P_i = 0$, the refraction law in Eq. (3.18), which must be implemented at the bubble surface $r = R(\tau)$, is

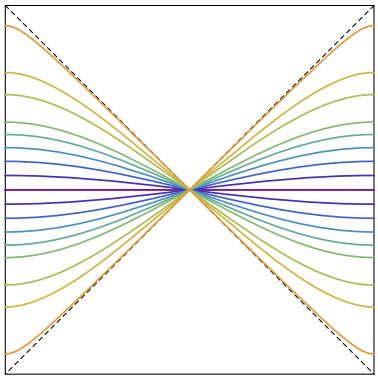

FIG. 10. Examples of extremal codimension one surfaces with $P_i = 0$ in the dS Penrose diagram. The interior part of the smooth extremal surfaces correspond to the portion of these surfaces inside the bubble.

$$\frac{R}{\sqrt{f_i(R)}} = \frac{\rho_o(R)}{f_o(R)} + \frac{dT_o}{dR} P_o,$$
$$P_o = \pm\sqrt{\rho_o^2(R) - f_o(R)R^2}. \tag{4.2}$$

Depending on the sign of the product $\frac{dT_o}{dR} P_o$, two physically different solutions to the constraint (4.2) exist. Let us fix for convenience the sign in Eq. (2.24) as follows

$$\frac{dT_o}{dR} = -\frac{1}{2\kappa} \frac{w_o(R)}{(R^2 - \mu)\sqrt{AR^4 - BR^2 + C}},$$
$$w_o(R) = 1 + \mu - R^2(1 + \lambda + \kappa^2). \tag{4.3}$$

Note that[2] the quantity $w_o(R_{\max})$ is positive for $0 < \mu < \mu_s$ and negative for $\mu_s < \mu < \mu_0$. In both cases, the sign choice in Eq. (4.3) is such that, for $T_o \ge 0$, the bubble always moves toward the upper direction of the Penrose diagram. The configuration in which the bubble moves in the opposite direction can be recovered by a time reflection $t \to -t$.

With the assumption of positive P_o, Eq. (4.2) has the following solution

$$\rho_o(R) = -\frac{R(\mu - 1 + R^2(\kappa^2 + \lambda - 1))}{2\sqrt{1 - \lambda R^2}}. \tag{4.4}$$

From a direct calculation, we can check that $\rho_o(R_{\max})$ vanishes just for $\mu = \mu_s$. Also, we have that $\rho_o(R_{\max}) > 0$ for $\mu \to 0$. This shows that $\rho_o(R_{\max})$ is positive for $0 < \mu < \mu_s$ and negative for $\mu_s < \mu < \mu_0$. In both cases, this sign is consistent with a refraction of the extremal surface through the domain wall. For negative P_o, the solution to

[2]This can be checked by the following properties: (a) the unique positive solution of the equation $w_o(R_{\max}) = 0$ in the variable μ is $\mu = \mu_s$; (b) for $\mu = 0$, $w_o(R_{\max}) > 0$.

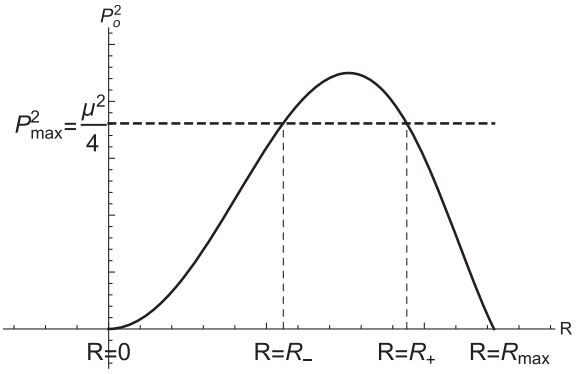

FIG. 11. Behavior of $P_o^2(R)$ in Eq. (4.5) for small bubbles.

Eq. (4.2) corresponds to a "reflection" of the extremal surface, see Appendix C 1. Thus, we discard this solution.

Plugging Eq. (4.4) into Eq. (4.2), we get

$$P_o^2(R) = R^2(\mu - R^2) + \frac{1}{4}R^2\frac{(\mu - 1 + R^2(\kappa^2 + \lambda - 1))^2}{1 - \lambda R^2}, \tag{4.5}$$

see Fig. 11 for a plot. Note that $P_o^2(0) = P_o^2(R_{\max}) = 0$. Using the fact that $R < 1/\sqrt{\lambda}$ for small bubbles, we obtain the following inequality

$$P_o^2(R) \geq U_o(R) = R^2(\mu - R^2), \tag{4.6}$$

where $U_o(R)$ is the effective potential in Eq. (3.8). The maximum of $U_o(R)$ is at $R = \hat{R} = \sqrt{\mu/2}$ and its value is $U_o(\hat{R}) = \mu^2/4 = P^2_{\max}$, defined in Eq. (3.11). Then, the maximum of $P_o^2(R)$ is bigger than $P^2_{\max}$, as it is clear from Fig. 11. Let us define the radii $R_\pm$ as the two solutions to the equation

$$P_o^2(R_\pm) = P^2_{\max} = \frac{\mu^2}{4}. \tag{4.7}$$

From the property $P_o^2(\sqrt{\mu/2}) > \mu^2/4$, it follows that

$$R_- \leq \sqrt{\frac{\mu}{2}} \leq R_+. \tag{4.8}$$

As we will see, the radii $R_\pm$ determine the behavior of the complexity rate at large time t_b.

1. Complexity rate

Depending on the parameter values and on R, the quantity $\rho_o(R)$ in Eq. (4.4) can be either positive or negative. A detailed analysis is deferred to Appendix C 2. Based on the sign of $\rho_o(R)$, the details of the extremal surface are slightly different. Let us distinguish between the two situations:

(i) $\rho_o(R) > 0$. The radial coordinate of the extremal surface is monotonic between $r = R$ and the AdS UV cutoff $r = \Lambda$. From Eq. (3.14), the volume is

$$\frac{\mathcal{V}}{2\pi} = \int_0^R \frac{r}{\sqrt{f_i(r)}}dr + \int_R^\Lambda \frac{r^2}{\sqrt{P_o^2 + f_o(r)r^2}}dr. \tag{4.9}$$

According to Eq. (3.13), the boundary time is

$$t_b = T_o(R) - \int_R^\Lambda \frac{1}{f_o}\left(\frac{P_o}{\sqrt{P_o^2 + f_o(r)r^2}}\right)dr. \tag{4.10}$$

In order to find the complexity rate, we use the same strategy as in [83]. Namely, we sum and subtract the quantity $P_o t_b$ to the volume expressed in Eq. (4.9):

$$\frac{\mathcal{V}}{2\pi} = P_o t_b + \int_0^R \frac{r}{\sqrt{f_i(r)}}dr + \int_R^\Lambda \frac{\sqrt{P_o^2 + f_o r^2}}{f_o}dr - P_o T_o(R). \tag{4.11}$$

Taking the derivative of Eq. (4.11) with respect to t_b, and using Eq. (4.2), we find the complexity rate

$$W = \frac{1}{2\pi}\frac{d\mathcal{V}}{dt_b} = P_o. \tag{4.12}$$

The asymptotic linear growth corresponds to the $\mathcal{V} \to \infty$ and $t_b \to \infty$ limit, which formally comes from the divergence of the integrands in Eqs. (4.9) and (4.10) in correspondence of the turning point $r_{t,\mathrm{AdS}}$, see Eq. (3.10). In particular, the turning point $r_{t,\mathrm{AdS}}$ satisfies

$$P_o^2 + f_o r^2 = 0.$$

This singularity is integrable except for $P_o^2 \to P^2_{\max} = \mu^2/4$. In order to find a divergent t_b in Eq. (4.10), we need the turning point $r_{t,\mathrm{AdS}} = \sqrt{\mu/2}$ to lie inside the integration domain $[R, \infty]$. Thus, from Eq. (4.8), we find that t_b is regular for $R \to R_+$ and diverges for $R \to R_-$. In other words, the late time limit $t_b \to \infty$ corresponds to $R \to R_-$.

(ii) $\rho_o(R) < 0$. For the extremal surfaces to be attached to the AdS boundary there must be a turning point $r_{t,\mathrm{AdS}} < R$ inside the black hole. From Eq. (3.14), the volume is

$$\frac{\mathcal{V}}{2\pi} = \int_0^R \frac{r}{\sqrt{f_i(r)}}dr - \int_R^{r_{t,\mathrm{AdS}}} \frac{r^2}{\sqrt{P_o^2 + f_o(r)r^2}}dr + \int_{r_{t,\mathrm{AdS}}}^\Lambda \frac{r^2}{\sqrt{P_o^2 + f_o(r)r^2}}dr. \tag{4.13}$$

According to Eq. (3.13), the boundary time reads

$$t_b = \int_R^{r_{t,\mathrm{AdS}}} \frac{1}{f_o}\left(\frac{P_o}{\sqrt{P_o^2 + f_o(r)r^2}}\right)dr - \int_{r_{t,\mathrm{AdS}}}^{\Lambda} \frac{1}{f_o}\left(\frac{P_o}{\sqrt{P_o^2 + f_o(r)r^2}}\right)dr + T_o(R). \tag{4.14}$$

The rate W can be evaluated by the same strategy as in the previous case. The result is again given by Eq. (4.12).

As in the previous case, the asymptotic linear growth of complexity is in correspondence of the divergence of the integrands in Eq. (4.14) at $r = r_{t,\mathrm{AdS}}$. The singularity is generally integrable, except for $P_o = P_{\max}$, for which $r_{t,\mathrm{AdS}} = \sqrt{\mu/2}$. In this case, the late t_b limit corresponds to $R \to R_+$. For $0 < R < R_+$, instead, the extremal surface never reaches the AdS boundary.

Extremal surfaces can be found numerically by integrating the equations of motion (3.7) and (3.8). The dS portion of these extremal surfaces corresponds to the $P_i = 0$ surfaces shown in Fig. 10. The AdS portion of two prototypical examples of solutions is plotted in the left panels of Figs. 12 and 13. The complexity rate as a function of the boundary time t_b is shown on the right panels of the same figures.

In the example in Fig. 12, for a given value of the boundary time t_b there exists a single extremal surface anchored at the AdS boundary. Instead, in the example in Fig. 13 in a time window centered at $t_b = 0$, i.e.

$$-T_b < t_b < T_b, \tag{4.15}$$

three extremal surfaces anchored at the same value of the boundary time t_b exist. The rate W is then a multivalued function of the time t_b.

To discriminate between the two possible behaviors, it is useful to introduce the quantity

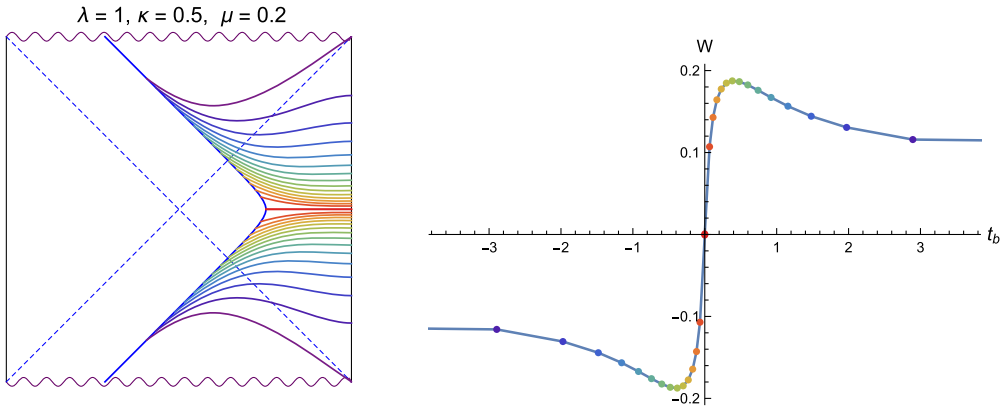

FIG. 12. Left panel: AdS portion of the extremal surfaces for a very small bubble. Right panel: plot of the complexity rate. For every value of the boundary time t_b there exists a single extremal surface.

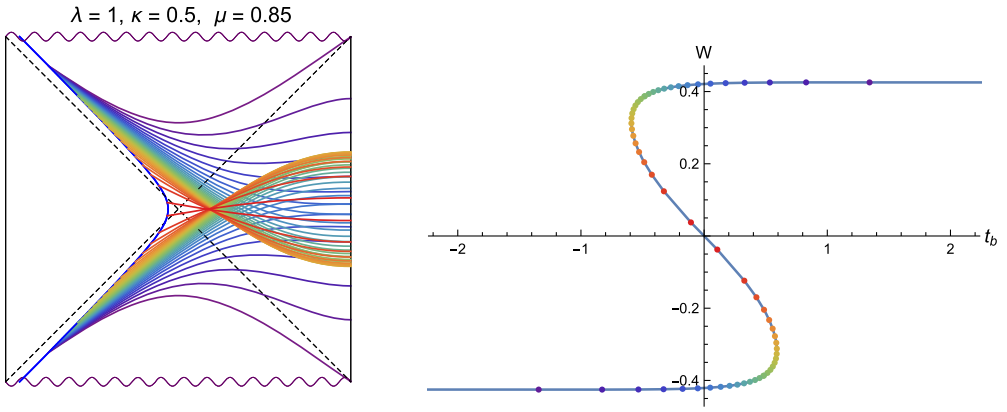

FIG. 13. Left panel: AdS portion of the extremal surfaces for a not so small bubble. Right panel: plot of the complexity rate. Note that multiple extremal surfaces exist for boundary times t_b inside the window in Eq. (4.15).

$$K = \left.\frac{dt_b}{dP_o}\right|_{t_b=0}, \tag{4.16}$$

representing the reciprocal of the slope $\frac{dW}{dt_b}$ computed at the origin of the plots in the right panel of figures 12 and 13. The complexity rate in Fig. 12 is characterized by $K > 0$, contrary to the one in Fig. 13, where $K < 0$. An explicit expression for K is given in Appendix C 3. From Eqs. (C8) and (C11), we find that K is a decreasing function of μ at fixed λ and κ and that $K \to -\infty$ for $\mu \to \mu_0$. In Fig. 14, we show K as a function of μ for a fixed value of λ and κ. In the parameter region

$$\lambda \geq 2 + \kappa - \kappa^2, \tag{4.17}$$

the quantity K is always negative, so multiple extremal surfaces exist for every μ, see Fig. 15.

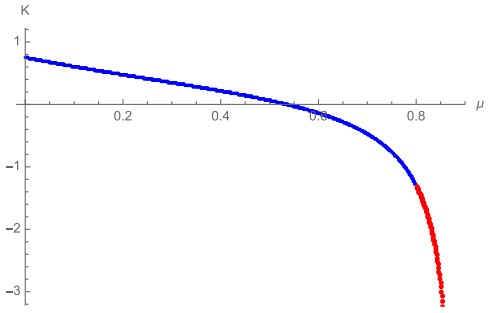

FIG. 14. Plot of the quantity K defined in Eq. (4.16) as a function of μ for $\lambda = 1$, $\kappa = 0.5$. In this numerical example K is negative for $\mu > 0.53$ and approaches $-\infty$ for $\mu \to \mu_0 \approx 0.88$. In order to have multiple extremal surface for the same value of t_b as in Fig. 13, we need $K < 0$. The blue portion of the plot corresponds to very small bubbles, while the red part to not so small bubbles.

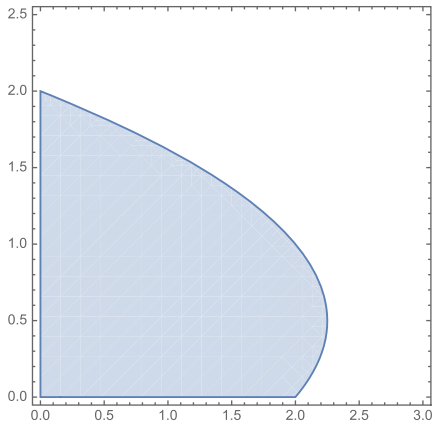

FIG. 15. The white region represents the portion of the (λ, κ) plane defined in Eq. (4.17), for which K is negative for every value of μ.

According to the CV conjecture, when multiple extremal surfaces exist, the one with maximal volume should be picked. To deal with this, let us consider the prototypical behavior shown in Fig. 16. The three points C, D, and E are obtained by extremal surfaces anchored at the same boundary time, but whose volumes $\mathcal{V}$ and values of the rate differ. To properly choose the maximal solution, let us first consider the two points C and D. The volumes $\mathcal{V}_C$ and $\mathcal{V}_D$ of the corresponding surfaces can be inferred by starting from the volume $\mathcal{V}_A$ of the surface located at the point A, and following the two arrows which bring to C and D, respectively. Since the rate is positive, the volume increases as we move along these arrows. Hence, both $\mathcal{V}_C$ and $\mathcal{V}_D$ are higher than $\mathcal{V}_A$. Precisely, since the growth rate as we move from A to C is larger than the one going from A to D, we conclude that $\mathcal{V}_C > \mathcal{V}_D$. Moreover, by time-reversal symmetry, $\mathcal{V}_C = \mathcal{V}_F$. Moving along the curve from E to F the rate is negative, which means that the volume is decreasing: $\mathcal{V}_F < \mathcal{V}_E$. From this argument, we should choose the lowest value of the rate for $t_b < 0$ and the highest value of the rate for $t_b > 0$, see Fig. 17. Consequently, the complexity rate W experiences a discontinuous jump at $t_b = 0$. A similar analysis was performed in [63] for complexity in dS spacetime.

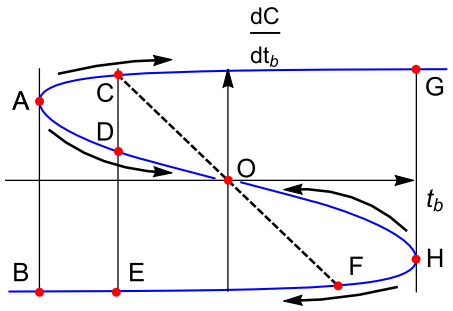

FIG. 16. Schematic plot of the complexity rate in the parameter region where there are multiple extremal surfaces anchored at the same boundary time.

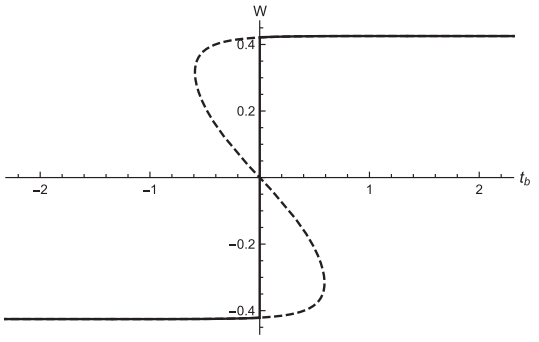

FIG. 17. The requirement of maximal volume selects the steplike function rate represented by the solid line.

2. Late time complexity rate

We now discuss the late time behavior of the rate W. In terms of the bubble radius, we will show that $t_b \to \infty$ corresponds to $R \to R_+$ or to $R \to R_-$, depending on the point in the parameter space. First note that $\rho_o(R_+)$ has the same sign as $\rho_o(R_-)$. In fact, if the signs of $\rho_o(R_\pm)$ were different, we would have $R_- < R_0 < R_+$, where R_0 is defined by the condition $\rho_o(R_0) = 0$, see Eq. (C2). Then we should have $P_o^2(R_0) > \frac{\mu^2}{4}$, see Fig. 11, but this is impossible because

$$P_o^2(R_0) - \frac{\mu^2}{4} = -\frac{(\kappa^2\mu + \lambda\mu + \mu - 2)^2}{4(\kappa^2 + \lambda - 1)^2} \leq 0. \tag{4.18}$$

We can then check that the $t_b \to \infty$ limit corresponds to $R \to R_+$ or to $R \to R_-$. In particular, we can have

(i) Case 1: If $\rho_o(R_+) < 0$, the $t_b \to \infty$ limit corresponds to $R \to R_+$. In this case both the integrals in Eq. (4.14) diverge, due to a singularity in correspondence of $r_{t,\mathrm{AdS}}$. For large enough $t_b > 0$ the complexity rate is an increasing function of time (see for example the right panel of Fig. 13).

(ii) Case 2: If $\rho_o(R_+) > 0$, then also $\rho_o(R_-) > 0$. From Eq. (3.10), both for $R = R_+$ and $R = R_-$, we have that $r_{t,\mathrm{AdS}} = \sqrt{\mu/2}$, because $P_o^2 = \mu^2/4$. The integral which gives t_b, see Eq. (4.10), is then divergent for $R = R_-$ and not for $R = R_+$, because $R_- \leq r_{t,\mathrm{AdS}} \leq R_+$, see Eq. (4.8). In this case, at large enough $t_b > 0$ the complexity rate is a decreasing function of time, see for example the right panel of Fig. 12.

Either way, the complexity rate at late time is insensitive to the presence of the bubble

$$\frac{1}{2\pi} \lim_{t_b \to \infty} \frac{d\mathcal{V}}{dt_b} = \frac{\mu}{2}. \tag{4.19}$$

However, the sign of $\rho_o(R_+)$ discriminates between a growing or a decreasing complexity rate at late time. It is a complicated problem to discuss the sign of $\rho_o(R_+)$ in a generic point of the parameter space. Still, in some particular regions of parameters we can determine the sign of $\rho_o(R_+)$ with some simple arguments. For example, for $\mu \to 0$ we are always in case 2, because in this limit

$$R_+ \to R_{\max}, \qquad \rho(R_+) \to \frac{1}{(\kappa + 1)^2 + \lambda} > 0. \tag{4.20}$$

Instead, depending on the value of λ and κ, for $\mu \to \mu_0$ we can have both case 1 (for example $\lambda = 0.5$, $\kappa = 0.5$) and case 2 (for example $\lambda = 1$, $\kappa = 1$). See Appendix C 2 for further details.

According to the Lloyd's bound [84], the maximum allowed growth rate of quantum computational complexity should be proportional to the total energy. In quantum systems with holographic duals, it was proposed [57] that the Lloyd's bound is saturated at late time by the uncharged planar black hole solutions in AdS. In the parameter space portion of case 2 this version of the proposal is violated, because the asymptotic value is approached from above. Violations of the Lloyd's bound have been previously found for the CA conjecture, see [83,85–89]. In holographic models including just AdS boundaries, we do not know about any other violation of the bound for the CV proposal. See [90,91] for examples of AdS hairy black holes in which the bound is instead satisfied.

B. Large bubbles

Contrary to small bubbles, for large bubbles the dS part of the geometry contains the region beyond the cosmological horizon $r = 1/\sqrt{\lambda}$. However, recalling that $P_i = 0$, we point out that extremal codimension-one surfaces in the dS part cannot enter the region with $r > 1/\sqrt{\lambda}$, where the potential U_i is positive, see Fig. 9. Therefore, the extremal surfaces are confined into the static patches. In particular, for $0 < \mu < \mu_h$ the extremal surfaces extend into the right static patch. Since in this case the domain wall never enter the left static patch, we necessarily have $\rho_i(R) < 0$. On the other hand, for $\mu > \mu_h$ no portion of the right static patch is present in the geometry, so the extremal surfaces remain into the left static patch. From this argument we conclude that $\rho_i(R) > 0$.

Some technical details in the calculations slightly differ in the two cases:

(i) Very large bubble, $0 < \mu < \mu_h$. Equation (4.2), which determines P_o, is replaced by

$$-\frac{R}{\sqrt{f_i}} = \frac{1}{f_o}\rho_o + \frac{dT_o}{dR}P_o,$$
$$P_o = \pm\sqrt{\rho_o^2(R) - f_o(R)R^2}. \tag{4.21}$$

We fix the sign of Eq. (2.24) as in Eq. (4.3). The solution for positive P_o is

$$\rho_o = \frac{R(\mu - 1 + R^2(\kappa^2 + \lambda - 1))}{2\sqrt{1 - \lambda R^2}}. \tag{4.22}$$

From here, we obtain the same value of P_o as in Eq. (4.5). It can be checked that $\rho_o(R_{\min})$ in Eq. (4.22) is always negative. Also, for fixed λ, κ, and μ, $\rho_o(R)$ is a decreasing function of R. Therefore, $\rho_o(R)$ is always negative, which means that there is a turning point $r_{t,\mathrm{AdS}} < R$ in AdS. Note that $\rho_o(R) \to -\infty$ for $R \to 1/\sqrt{\lambda}$.

The extremal surface always crosses the dS horizon on the bifurcation sphere, because $P_i = 0$. Consequently, the volume is given by

$$\frac{\mathcal{V}}{2\pi} = \int_0^{\frac{1}{\sqrt{\lambda}}} \frac{r}{\sqrt{f_i(r)}} dr - \int_{\frac{1}{\sqrt{\lambda}}}^{R} \frac{r}{\sqrt{f_i(r)}} dr - \int_R^{r_{t,\mathrm{AdS}}} \frac{r^2}{\sqrt{P_o^2 + f_o(r) r^2}} dr + \int_{r_{t,\mathrm{AdS}}}^{\Lambda} \frac{r^2}{\sqrt{P_o^2 + f_o(r) r^2}} dr. \tag{4.23}$$

The boundary time t_b can be obtained by Eq. (4.14). We find that the complexity rate is again given by Eq. (4.12).

(ii) Not so large bubble, $\mu_h < \mu < \mu_0$. Equation (4.2) still holds. We fix the sign of Eq. (2.24) as in Eq. (4.3), in which $w_o(R)$ is always negative.[3] This choice corresponds to a bubble which, for $T_o \geq 0$, moves in the lower direction of the Penrose diagram. Assuming P_o to be positive,[4] the ρ_o solution is given by Eq. (4.4).

The quantity $\rho_o(R)$ changes sign at $R = R_0$, given in Eq. (C2). However, for $\mu > \mu_h$ we have $R_0 < R_{\mathrm{min}}$. In addition, in the present case the equation $\rho_o(R_{\mathrm{min}}) = 0$ has no solution, so $\rho_o(R_{\mathrm{min}})$ is always negative, in accordance with the refraction interpretation. Putting all together, we conclude that $\rho_o(R)$ remains negative in the range $R_{\mathrm{min}} < R < 1/\sqrt{\lambda}$. In particular, for $R \to 1/\sqrt{\lambda}$ we get $\rho_o \to -\infty$.

Due to the negativity of $\rho_o(R)$, there is a turning point at $r_{t,\mathrm{AdS}} < R$ in the AdS portion. We can then use Eq. (4.13) for the volume, Eq. (4.14) for the boundary time, and Eq. (4.12) for the complexity rate. The value of P_o^2 is still given by Eq. (4.5). From a direct calculation

$$P_o(R_{\mathrm{min}}) = 0, \qquad P_o(1/\sqrt{\lambda}) = \infty. \tag{4.24}$$

Moreover, for $R_{\mathrm{min}} < R < 1/\sqrt{\lambda}$, P_o is a monotonic function, a plot of which is displayed in Fig. 18. The unique solution R^* to the equation

$$P_o^2(R^*) = P_{\mathrm{max}}^2 = \mu^2/4, \tag{4.25}$$

with $R_{\mathrm{min}} < R^* < 1/\sqrt{\lambda}$, corresponds to the extremal surface at $t_b \to \infty$.

In Figs. 19 and 20 we show the extremal surfaces and the complexity rate for a very large and a not so large bubble, respectively. In these examples, a single extremal surface exists for any given boundary time t_b and the complexity rate is an increasing function of time.

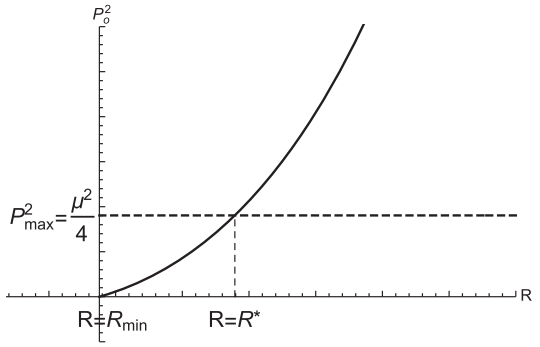

FIG. 18. Behavior of $P_o^2(R)$ in Eq. (4.5) for large bubbles.

In order to check if multiple extremal surfaces can emerge for a given t_b, we look at the behavior of K, expressed in Eq. (C12). A plot of K as a function of μ for fixed λ and κ is shown in Fig. 21. From the discussion below Eq. (C13), we find that for large bubbles K is always positive, thus there are no multiple extremal surfaces attached at the same boundary time.

The complexity rate at large t_b is still given by Eq. (4.19). The rate is always an increasing function of t_b at late time, because $P_o^2(R)$ is always an increasing function of R in the range $R_{\mathrm{min}} \leq R \leq R^*$, see Fig. 18. Referring to Sec. IV A 2, the late time rate of complexity behaves as in case 1 of small bubbles.

C. Static bubble limit

For the strictly static bubble configuration $\mu = \mu_0$, Eq. (B13) tells us that $P_o = 0$, so the complexity rate identically vanishes. In this setup, the time-translation symmetry is not broken by the presence of the bubble and $\partial/\partial t$ is an everywhere well-defined Killing vector. Also, the extremal surfaces never enter the black and white hole regions of the AdS geometry (see Fig. 22).

Let us now comment on how the static bubble is realized as a limit of the small and large bubbles:

(i) As μ approaches the critical value μ_0 from the small bubble direction, the time T_b in Eq. (4.15) tends to $+\infty$, and the slope of the complexity rate in the central unstable branch tends to zero, see Fig. 23. This is consistent with $K \to -\infty$ for $\mu \to \mu_0$, as shown in Fig. 14. In the static bubble limit $\mu \to \mu_0$, just the central branch solution survives and the complexity rate is zero. Interestingly, this limit is discontinuous, since the central branch is discarded by the maximum volume prescription, as indicated by the dashed line in Fig. 16.

(ii) As μ approaches the static bubble value μ_0 from the large bubble direction, at small t_b the complexity rate grows very slowly, see Fig. 24. When $\mu \to \mu_0$, the complexity rate remains frozen at zero for a large

[3] As $w_o(R)$ is a decreasing function of R, it is enough to check this property for $R = R_{\mathrm{min}}$, see Eq. (C15).

[4] If P_o is negative, ρ_o is given by Eq. (C1). This solution corresponds to a reflection, so we discard it.

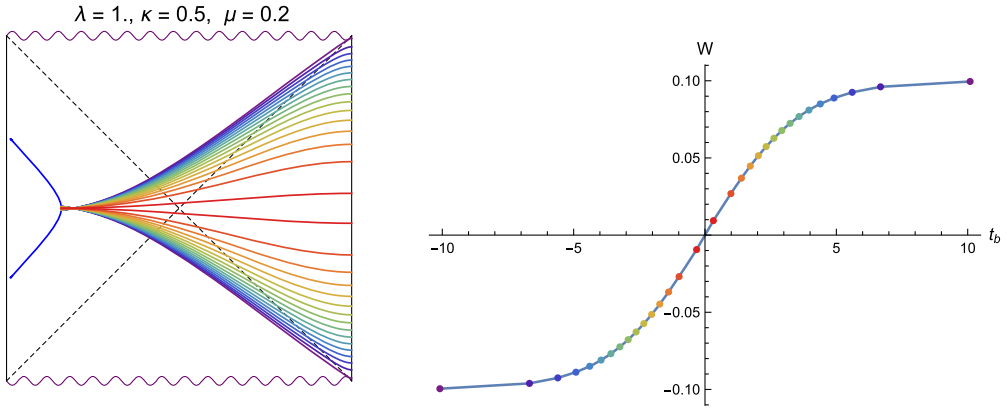

FIG. 19. Left panel: AdS portion of the extremal surfaces for an example of very large bubble. Right panel: plot of the complexity rate.

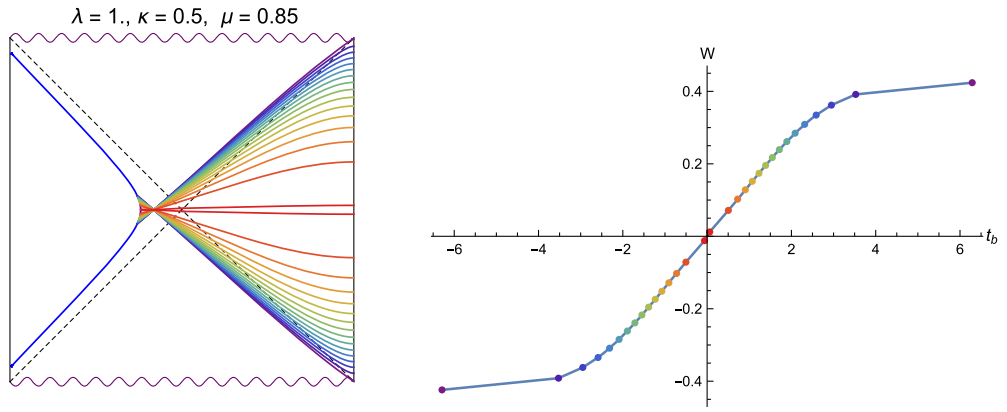

FIG. 20. Left panel: AdS portion of the extremal surfaces for an example of not so large bubble. Right panel: plot of the complexity rate.

time. This is consistent with K diverging to $+\infty$ in this limit, as shown in Fig. 21.

D. Complexity of formation

While it is possible to look at the collapse of a very small bubble from the outside of the black hole, for all the other kinds of bubble an external observer just see a black hole horizon. Thus, we can ask whether complexity can help us to discriminate, for a given value of the boundary time t_b, between a large and small bubble state with the same μ. To look for an answer, we consider the complexity of formation [92] at $t_b = 0$, at which time $P_i = P_o = 0$.

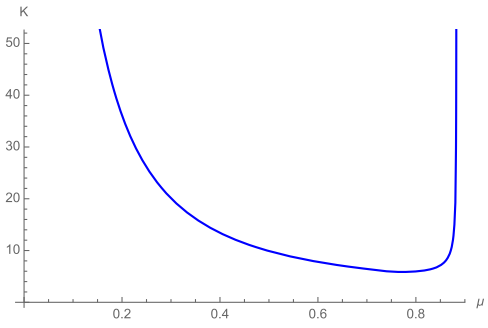

FIG. 21. Plot of K, defined in Eq. (4.16), as a function of μ for $\lambda = 1$ and $\kappa = 0.5$ in the case of large bubbles.

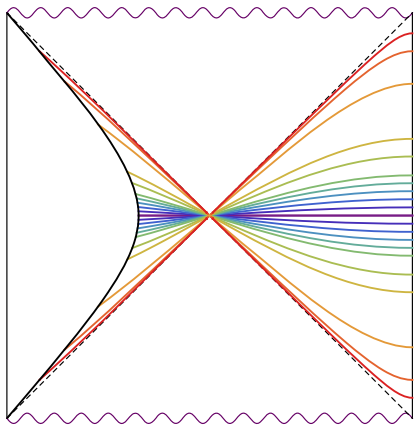

FIG. 22. AdS portion of the extremal solution for the static bubble (which is shown in the black solid line). These surfaces have all $P_o = 0$ and never enter the black and white hole regions of the geometry.

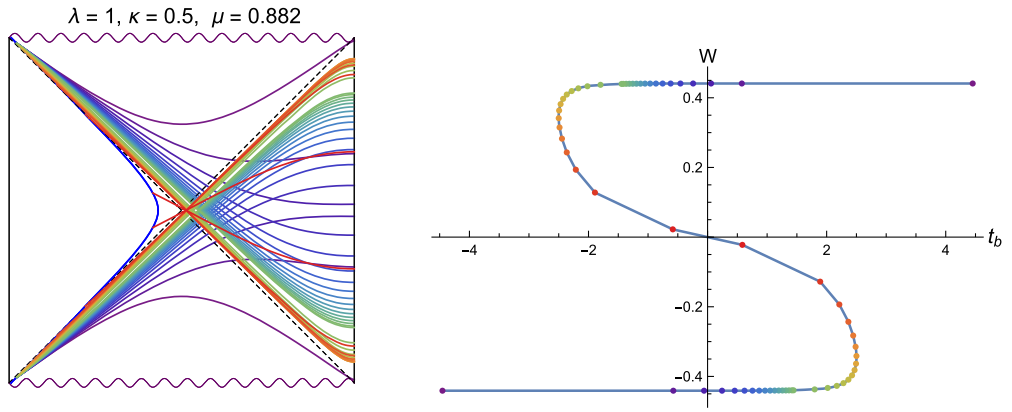

FIG. 23. Left panel: AdS portion of the extremal surfaces for a not so small bubble. The value of μ is rather close to the static bubble configuration, which, with the chosen values of λ and κ, is realized for $\mu_0 \approx 0.88278$. Right panel: plot of the complexity rate.

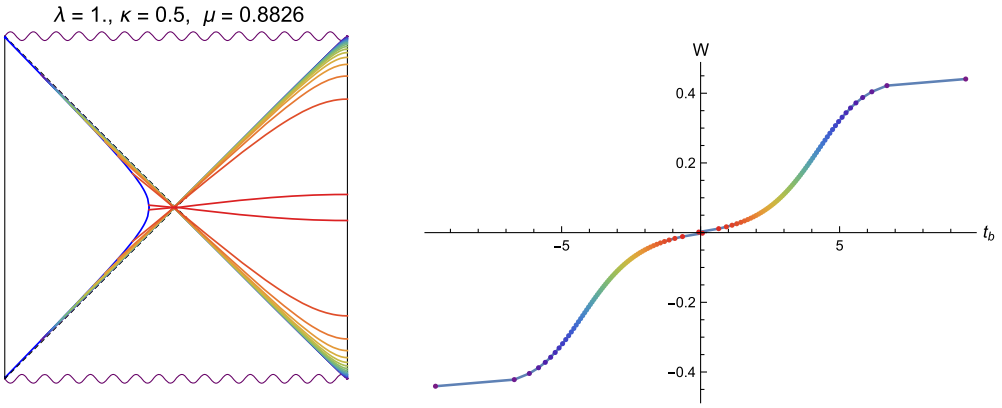

FIG. 24. Left panel: AdS portion of the extremal surfaces for an example of not so large bubbles with a μ rather close to the static bubble value $\mu_0 \approx 0.88278$. Right panel: plot of the complexity rate.

To get a finite quantity, we subtract from the volume of the bubble $\mathcal{V}_{\text{large}}$ (or $\mathcal{V}_{\text{small}}$) at $t_b = 0$ the outside volume of the BTZ black hole at the same boundary time:

$$\mathcal{V}_{\text{BTZ}} = 2\pi \int_{\sqrt{\mu}}^{\Lambda} \frac{r}{\sqrt{f_o}} dr = 2\pi\sqrt{\Lambda^2 - \mu} = 2\pi\Lambda + O\left(\frac{1}{\Lambda}\right), \tag{4.26}$$

where Λ is the AdS UV cutoff. The complexity of formation is thus proportional to

$$\Delta\mathcal{V}_{\text{large}} = \mathcal{V}_{\text{large}} - \mathcal{V}_{\text{BTZ}}, \qquad \Delta\mathcal{V}_{\text{small}} = \mathcal{V}_{\text{small}} - \mathcal{V}_{\text{BTZ}}. \tag{4.27}$$

From a direct evaluation from Eqs. (4.9), (4.13), and (4.23), we find

$$\frac{\Delta\mathcal{V}_{\text{small}}}{2\pi} = \frac{1 - \sqrt{1 - R_{\text{max}}^2\lambda}}{\lambda} \mp \sqrt{R_{\text{max}}^2 - \mu} \tag{4.28}$$

where the $\mp$ sign refers to the cases $0 < \mu < \mu_s$ and $\mu_s < \mu < \mu_0$, respectively. The regularized volume of large bubbles instead is

$$\frac{\Delta\mathcal{V}_{\text{large}}}{2\pi} = \sqrt{R_{\text{min}}^2 - \mu} + \frac{1 \pm \sqrt{1 - R_{\text{min}}^2\lambda}}{\lambda} \tag{4.29}$$

where the $\pm$ sign refers to the cases $0 < \mu < \mu_h$ and $\mu_h < \mu < \mu_0$, respectively.

A plot of $\Delta\mathcal{V}_{\text{large}}$ and $\Delta\mathcal{V}_{\text{small}}$ as function of μ is shown in Fig. 25. The large bubble has always a larger complexity than the small one. This confirms the intuition that a large bubble state is more complex compared to a small bubble one with the same mass. Also, $\Delta\mathcal{V}_{\text{small}}$ is negative for $\mu \to 0$. Very small bubbles in the limit $\mu \to 0$ then correspond to less complex states compared to the BTZ eternal black hole.

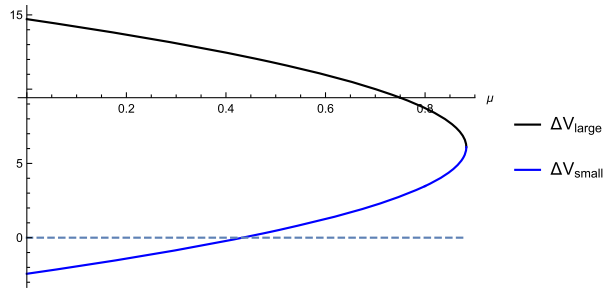

FIG. 25. Plot of $\Delta\mathcal{V}_{\rm small}$ and $\Delta\mathcal{V}_{\rm large}$ in Eqs. (4.28) and (4.29) as functions of μ, for $\lambda = 1$ and $\kappa = 0.5$.

V. COMPLEXITY WITH A DS STRETCHED HORIZON

For a very large bubble with $0 < \mu < \mu_h$, the geometry includes a complete dS stretched horizon. Consequently, we can consider a different prescription to compute volume complexity, in which the extremal codimension one surface is attached both to the AdS boundary and to the dS stretched horizon. This is an intermediate situation between the configuration used in the CV proposal in AdS [55] and in dS [24]. The stretched dS horizon is located at constant $r = r_{\rm sh}$, where

$$r_{\rm sh} = \frac{1}{\sqrt{\lambda}}(1-\epsilon), \tag{5.1}$$

and $\epsilon \to 0$ is the horizon cutoff. An $\epsilon > 0$ is necessary to define a notion of time on the dS boundary, as the horizon is a null hypersurface for $\epsilon = 0$.

We choose the parameter l in Eq. (3.2) in such a way that it is positive and that $r(l=0) = r_{\rm sh}$. The dS boundary removes the conical singularity presented by extremal surfaces at the center of the static patch for $P_i \neq 0$. For this reason, we are allowed to consider an arbitrary value of P_i.

Extremal surfaces are stretched between the dS horizon and the AdS boundary, so we can define the left and the right boundary times t_L, t_R as the boundary conditions

$$\begin{aligned} t_L &= t_i(l=0), \quad \text{where } r(l=0) = r_{\rm sh} \\ t_R &= t_o(l=l_\Lambda), \quad \text{where } r(l=l_\Lambda) = \Lambda \end{aligned} \tag{5.2}$$

and Λ is the AdS UV cutoff. In the definition of the boundary time, we consider an arbitrary linear relation between t_L and t_R

$$t_L = \alpha_t t_R, \tag{5.3}$$

where α_t is some opportune numerical constant. The boundary time t_b then is

$$t_b = -t_L = -\alpha_t t_R. \tag{5.4}$$

As a technical difference compared to the usual Kruskal extension of the AdS black hole, there is no time-translation Killing vector ∂_t which is globally defined in all the geometry, because time invariance is broken by the trajectory of the bubble. If such a symmetry existed, it would provide an appropriate value of α_t which would give a zero complexity rate. We then expect a nontrivial time dependence of complexity for every value of α_t.

A. Extremal surfaces

In the AdS part of the geometry, the domain wall is located into the left exterior of the black hole. Thus, for the extremal surface to cross the black or white hole interior, we must require $\rho_o(R) < 0$. Instead, the sign of $\rho_i(R)$ might be positive or negative. Explicitly,

$$\begin{aligned} \rho_o(R) &= -\sqrt{P_o^2 + f_o(R)R^2}, \\ \rho_i(R) &= \pm\sqrt{P_i^2 + f_i(R)R^2}. \end{aligned} \tag{5.5}$$

The condition for the extremal surface to reach the AdS boundary without falling into the black hole singularity is $-\mu/2 \le P_o \le \mu/2$ (see the plot of the potential in the right panel of Fig. 9). By time-reflection invariance, we take $P_o = P_i = 0$ at $t_b = 0$, when the extremal surface meets the domain wall at $R = R_{\rm min}$.

Under these assumptions, the matching condition in Eq. (3.18) reads

$$P_i \frac{dT_i}{dR} \pm \frac{\sqrt{P_i^2 + f_i(R)R^2}}{f_i(R)} = P_o \frac{dT_o}{dR} - \frac{\sqrt{P_o^2 + f_o(R)R^2}}{f_o(R)}, \tag{5.6}$$

where the $\pm$ sign corresponds to $\rho_i(R) > 0$ or $\rho_i(R) < 0$, respectively. We choose the sign of dT_o/dR as in Eq. (4.3), and the sign of dT_i/dR in Eq. (2.24) as follows

$$\begin{aligned} \frac{dT_i}{dR} &= -\frac{1}{2\kappa}\frac{w_i(R)}{(1-\lambda R^2)\sqrt{AR^4 - BR^2 + C}}, \\ w_i(R) &= 1 + \mu - R^2(1 + \lambda - \kappa^2). \end{aligned} \tag{5.7}$$

As a function of μ, the quantity $w_i(R_{\rm min})$ is positive for $\mu > \mu_h$ and negative for $\mu < \mu_h$. For $\mu = \mu_h$, $w_i(R_{\rm min})$ vanishes and the bubble initially sits exactly at the dS bifurcation point.

Equation (5.6) is solved by

$$\begin{aligned} P_i &= \frac{P_o(w_i w_o \pm \xi) + \sqrt{\xi}(w_i \pm w_o)\sqrt{P_o^2 + f_o R^2}}{4\kappa^2 R^2 f_o}, \\ \xi &= -4\kappa^2 V(R) R^2, \end{aligned} \tag{5.8}$$

where $V(R)$ is given in Eq. (2.14). We point out that the solution with $P_i = 0$ reproduces the smooth extremal surfaces studied in Sec. IV. The− sign describes an extremal surface experiencing a refraction, see Eq. (4.5), while the + sign denotes an extremal surfaces undergoing a reflection, see Eq. (C1). Specializing to the physical refracted solution, Eq. (5.8) can be further simplified to

$$P_i = \frac{1}{2f_o}\left(P_o(1-\mu+R^2(1-\lambda-\kappa^2)) + \sqrt{\xi}\sqrt{P_o^2+f_o R^2}\right). \tag{5.9}$$

An extremal surface is specified by the conserved quantities P_i and P_o, which are related by Eq. (5.9). Their values for given boundary times are fixed by the boundary condition in Eq. (5.3), as we will explain below.

For the extremal surface to reach the AdS boundary, the turning point defined in Eq. (3.12) must be at $r_{t,\mathrm{dS}} \geq R$, which holds true for

$$P_i^2 \geq \tilde{P}_i^2, \qquad \tilde{P}_i^2 = R^2(\lambda R^2 - 1). \tag{5.10}$$

For $R_{\min} < R < 1/\sqrt{\lambda}$, the domain wall is located on the right side of the dS static patch, so $\rho_i(R) < 0$. We may expect that at some point $R = \tilde{R} > 1/\sqrt{\lambda}$, whose location depends on the bubble parameters and on the choice of α_t, the function $\rho_i(R)$ vanishes. Then, $\rho_i(R) > 0$ for $R > \tilde{R}$.

The condition $\rho_i(\tilde{R}) = 0$ is equivalent to $P_i^2 = \tilde{P}_i^2$, see Eq. (5.10). In terms of P_o, this gives

$$P_o = \tilde{P}_o = \frac{R(\mu - 1 + R^2(\lambda + \kappa^2 - 1))}{2\sqrt{\lambda R^2 - 1}}, \tag{5.11}$$

which is well defined just for $R > 1/\sqrt{\lambda}$. Note that $\tilde{P}_o \to -\infty$ for $R \to 1/\sqrt{\lambda}$. For $R > 1/\sqrt{\lambda}$ and $P_o > \tilde{P}_o$ we have $\rho_i(R) < 0$, while for $P_o < \tilde{P}_o$ we have $\rho_i(R) > 0$.

B. Complexity

For the calculation of volume and boundary time, let us distinguish between two cases:

(i) $\rho_i(R) < 0$. The volume is given by

$$\begin{aligned}\frac{\mathcal{V}}{2\pi} = &\int_{r_{sh}}^{r_{t,\mathrm{dS}}} \frac{r^2}{\sqrt{P_i^2 + f_i(r)r^2}}\,dr \\ &- \int_{r_{t,\mathrm{dS}}}^{R} \frac{r^2}{\sqrt{P_i^2 + f_i(r)r^2}}\,dr \\ &- \int_{R}^{r_{t,\mathrm{AdS}}} \frac{r^2}{\sqrt{P_o^2 + f_o(r)r^2}}\,dr \\ &+ \int_{r_{t,\mathrm{AdS}}}^{\Lambda} \frac{r^2}{\sqrt{P_o^2 + f_o(r)r^2}}\,dr.\end{aligned} \tag{5.12}$$

From Eq. (3.13), we can write the following expression for the AdS boundary time

$$\begin{aligned}t_R = T_o(R) &+ \int_{R}^{r_{t,\mathrm{AdS}}} \frac{P_o}{f_o\sqrt{P_o^2 + f_o(r)r^2}}\,dr \\ &- \int_{r_{t,\mathrm{AdS}}}^{\Lambda} \frac{P_o}{f_o\sqrt{P_o^2 + f_o(r)r^2}}\,dr,\end{aligned} \tag{5.13}$$

and the following expression for the dS boundary time

$$\begin{aligned}t_L = T_i(R) &+ \int_{r_{\mathrm{sh}}}^{r_{t,\mathrm{dS}}} \frac{P_i}{f_i\sqrt{P_i^2 + f_i(r)r^2}}\,dr \\ &- \int_{r_{t,\mathrm{dS}}}^{R} \frac{P_i}{f_i\sqrt{P_i^2 + f_i(r)r^2}}\,dr.\end{aligned} \tag{5.14}$$

(ii) $\rho_i(R) > 0$. The volume can be written as

$$\begin{aligned}\frac{\mathcal{V}}{2\pi} = &\int_{r_{\mathrm{sh}}}^{R} \frac{r^2}{\sqrt{P_i^2 + f_i(r)r^2}}\,dr \\ &- \int_{R}^{r_{t,\mathrm{AdS}}} \frac{r^2}{\sqrt{P_o^2 + f_o(r)r^2}}\,dr \\ &+ \int_{r_{t,\mathrm{AdS}}}^{\Lambda} \frac{r^2}{\sqrt{P_o^2 + f_o(r)r^2}}\,dr.\end{aligned} \tag{5.15}$$

Equation (5.13) is still valid. Instead, from Eq. (3.13) we find that the time on the dS boundary is

$$t_L = T_i(R) + \int_{r_{sh}}^{R} \frac{P_i}{f_i\sqrt{P_i^2 + f_i(r)r^2}}\,dr. \tag{5.16}$$

In order to find values of P_i and P_o consistent with the boundary condition, we need to solve Eq. (5.3) where t_R and t_L are specified by (5.13) and (5.14) or (5.16), respectively. This integral equation can be solved numerically by the shooting method.

We can then compute the extremal surfaces and their volume numerically. In Fig. 26 we show the result for $\alpha_t = 1$, while in Fig. 27 we display the result for the choice $\alpha_t = -1$. In both cases we find a hyperfast complexity rate, because the volume of the extremal surface diverges for a finite value of the boundary time t_b.

C. Critical time behavior

Let us now discuss the limit of hyperfast complexity growth. Expanding Eq. (5.9) for large R, we find that

$$P_i(R) \approx \frac{\sqrt{(\lambda + (\kappa-1)^2)(\lambda + (\kappa+1)^2)}}{2} R^2 + O(R^0). \tag{5.17}$$

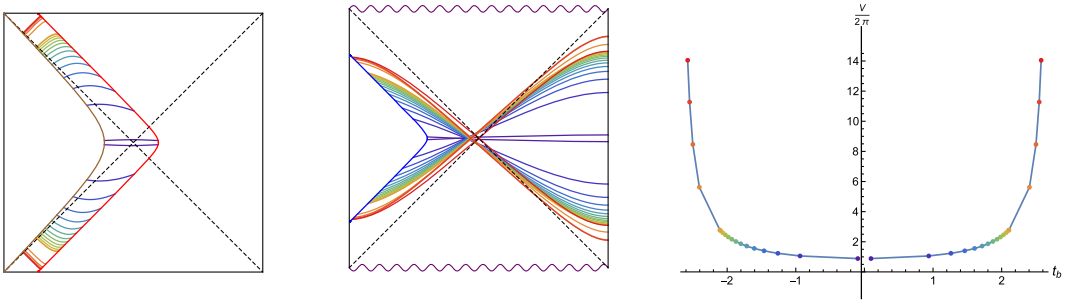

FIG. 26. Left and central panels: extremal surfaces in the dS and in the AdS portion of the Penrose diagram, respectively. Right panel: plot of the volume as a function of boundary time t_b. We set $\alpha_t = 1$, see Eq. (5.3), and we choose $\kappa = 0.2$, $\lambda = 1.5$, $\mu = 0.4$, and $\epsilon = 0.06$.

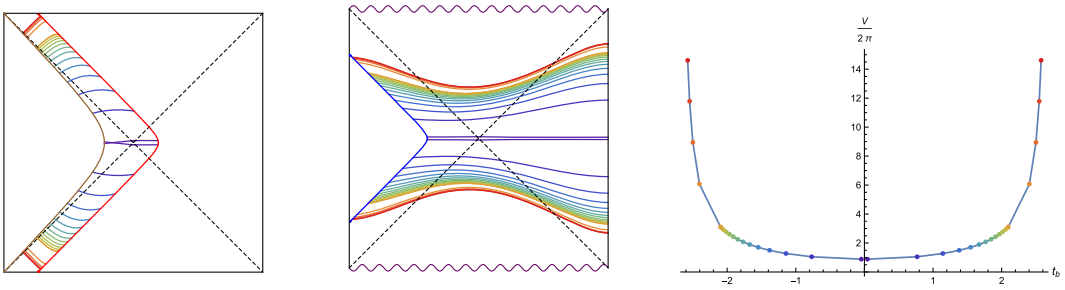

FIG. 27. Plots of the same quantities as in Fig. 26, with the choice $\alpha_t = -1$.

The dependence of P_i on P_o shows up just at order $O(R^0)$. At large R, we can approximate $T_i(R)$ in Eq. (2.24) as

$$\frac{dT_i}{dR} \approx \frac{1}{f_i}\frac{1+\lambda-\kappa^2}{\sqrt{(\lambda+\kappa^2-1)^2+4\lambda}},$$
$$T_i(R) \approx \frac{1+\lambda-\kappa^2}{\sqrt{(\lambda+\kappa^2-1)^2+4\lambda}} r_i^*(R) + Q, \qquad (5.18)$$

where Q is an integration constant. Note that $1+\lambda-\kappa^2 > 0$, because $\kappa < 1$ in the very large bubble regime.

Let us discriminate between two cases:

(i) $\lambda+\kappa^2 > 1$. At large R, from Eq. (5.11) we have $\tilde{P}_o \to +\infty$, then $\rho_i(R) > 0$. At large P_i, we can approximate Eq. (5.16) as

$$t_L \approx T_i(R) + \int_{r_{\rm sh}}^{R} \frac{dr}{f_i}$$
$$= T_i(R) + r_i^*(R) - r_i^*(r_{sh}), \qquad (5.19)$$

which gives

$$t_L \approx \omega\frac{1}{R\lambda} + Q - \frac{1}{4\sqrt{\lambda}}\log\frac{4}{\epsilon^2},$$
$$\omega = 1 + \frac{1+\lambda-\kappa^2}{\sqrt{(\lambda+\kappa^2-1)^2+4\lambda}}. \qquad (5.20)$$

In the above expression, we have $\omega > 0$ because for very large bubbles $\kappa < 1$. For large R, the dS part of the volume in Eq. (5.15) diverges linearly:

$$\frac{\mathcal{V}_{dS}}{2\pi} = \int_{r_{\rm sh}}^{R} \frac{r^2}{\sqrt{P_i^2 + f_i(r)r^2}}dr$$
$$\approx R\int_{\frac{r_{\rm sh}}{R}}^{1} \frac{y^2}{\sqrt{\frac{(\lambda+(\kappa-1)^2)(\lambda+(\kappa+1)^2)}{4} - \lambda y^4}}dy. \qquad (5.21)$$

The divergence of the volume for large R is at the value of t_L given in Eq. (5.20).

(ii) $\lambda+\kappa^2 < 1$. At large R we have $\tilde{P}_o \to -\infty$, which gives $\rho_i(R) < 0$. In this limit, combining Eq. (3.12) with Eq. (5.17), we find

$$r_{t,\rm dS} \approx \frac{R}{\sqrt{2}}\left(\frac{(\lambda+(\kappa-1)^2)(\lambda+(\kappa+1)^2)}{\lambda}\right)^{1/4}. \qquad (5.22)$$

At large R, corresponding to large P_i, we can approximate t_L in Eq. (5.14) as

$$t_L \approx T_i(R) + \int_{r_{\rm sh}}^{r_{t,\rm dS}} \frac{dr}{f_i} + \int_{R}^{r_{t,\rm dS}} \frac{dr}{f_i}, \qquad (5.23)$$

which gives

$$t_L \approx \tilde{\omega}\frac{1}{\lambda R} + Q - \frac{1}{4\sqrt{\lambda}}\log\frac{4}{\epsilon^2}, \tag{5.24}$$

where

$$\tilde{\omega} = \frac{2\sqrt{2}\lambda^{1/4}}{[(\lambda+(\kappa-1)^2)(\lambda+(\kappa+1)^2)]^{1/4}} + \frac{1+\lambda-\kappa^2}{\sqrt{(\lambda+\kappa^2-1)^2+4\lambda}} - 1. \tag{5.25}$$

In the case at hand, the quantity $\tilde{\omega}$ is always positive. At large R and at the finite time in Eq. (5.24), the volume again diverges linearly as in Eq. (5.21).

Summarizing, in both cases the volume complexity diverges for $t_b = t_{\rm cr}$, where the critical time is

$$t_{\rm cr} = \frac{1}{4\sqrt{\lambda}}\log\frac{4}{\epsilon^2} - Q, \tag{5.26}$$

and Q is the integration constant defined in Eq. (5.18). The divergence at $t_b = t_{\rm cr}$ takes place independently of the parameter α_t in Eq. (5.3). For $t_b > t_{\rm cr}$, no extremal surface exists which connects the left dS and right AdS boundaries. As in [63], we may regularize the divergence in the complexity rate by introducing a cutoff surface at large $r = r_{\rm cut}$ nearby the future dS infinity. With this regularization, the complexity rate would remain finite and at $t > t_{\rm cr}$ it would saturate at a value divergent in the UV cutoff $r_{\rm cut}$.

VI. CONCLUSIONS

In this paper we investigated the time dependence of volume complexity in a class of asymptotically AdS_3 spacetimes which include a dS_3 bubble in their interior. We first focused on extremal surfaces attached just at the AdS boundary and smooth everywhere into the interior spacetime. With the exception of the static bubble configuration, we found that complexity asymptotically grows linearly as a function of time, with the same rate as for the BTZ black hole. For large bubbles, the asymptotic value of the complexity rate is always reached from below. For small bubbles, the asymptotic limit can be instead reached either from below (case 1) or from above (case 2), depending on the parameter space (see Sec. IV A 2).

The static bubble configuration gives rise to a time-independent complexity, so it does not match the expectation, generically satisfied by AdS black holes, that complexity rate at late time is of the same order of magnitude as TS, with T the temperature and S the entropy of the system [34]. This fine-tuned solution, which is realized for $\mu = \mu_0$, interpolates between the small and the large bubble regimes. As soon as a small perturbation is introduced, the static bubble limit can be achieved in two different ways:

(i) If the limit $\mu \to \mu_0$ in the parameter space is approached from the large bubble configuration, the complexity rate remains frozen to zero for an initial amount of time which tends to infinity for $\mu \to \mu_0$, see the right panel of Fig. 24. From this side, the asymptotic complexity rate of the BTZ black hole is recovered in a continuous way after an arbitrarily large time.

(ii) If the limit $\mu \to \mu_0$ is approached from the small bubble region of the parameter space, the static behavior of complexity emerges from a class of extremal surfaces with nonmaximal volume, see Fig. 23. According to the CV prescription, the non-maximal extremal solutions should be discarded for $\mu \neq \mu_0$ in favor of the global maximum, as shown by the dashed line in Fig. 17. For $\mu \to \mu_0$ the complexity rate resembles a step function, thus the limit is discontinuous, as in a first order phase transition.

Interestingly, the discarded solutions would give rise to a negative complexity rate, as for the two-dimensional centaur geometries studied in [67]. We may contemplate the possibility that other physical configurations could exist, which resemble our geometry nearby the discarded extremal surfaces and in which the global maximum is cut away. If such a surgery were performed, it would give rise to a negative complexity rate, resembling the two-dimensional case studied in [67], in which no black hole horizon is present in the AdS region of the geometry.

With both procedures, for $\mu \to \mu_0$ the BTZ asymptotic complexity rate is recovered at late time. The limit is continuous from the large bubble direction, while it is discontinuous from the small bubble side. In this sense, the static bubble can be seen as a fine-tuned critical configuration separating qualitatively different behaviors in the parameter space.

From the point of view of local observables on the AdS boundary, the static bubble configuration is not distinguishable from the eternal BTZ black hole. The same holds for entanglement entropy of subregions located on the AdS boundary. To detect the discontinuous nature of the static bubble limit, other quantum information probes, such as holographic complexity, are required.

Contrary to the result found in [24,63] for dS, if we consider smooth extremal surfaces attached just to the AdS boundary there is no hyperfast growth of complexity. In Sec. V, we checked that hyperfast growth is recovered in the very large bubble case if we consider extremal surfaces anchored both at the AdS boundary and at the dS stretched horizon. This choice should correspond to complexity of a pure thermofield double state which involves both an AdS and a dS boundary. Defining the boundary time t_b as in Eq. (5.4), we find that the volume complexity diverges at

$t_b = t_{\rm cr}$ given in Eq. (5.26), independently of the parameter α_t in Eq. (5.3).

It is tempting to suggest the following interpretations for the two different ways to apply the CV conjecture in AdS geometries with very large dS bubbles:

(i) the volume of smooth extremal surfaces anchored just at the boundary of AdS is proportional to the complexity of a mixed CFT state, obtained by tracing over the dS degrees of freedom in the thermofield double state. This situation is reminiscent of the subregion complexity proposal [93–95].

(ii) the volume of the extremal surface anchored both at the AdS boundary and at the dS static patch horizon is proportional to the complexity of the pure product state.

Why the latter choice of boundary conditions is possible just for very large bubbles is an interesting question. Small bubble solutions do not contain a stretched horizon in the dS portion of the geometry, so the only implementable prescription is to attach the extremal surfaces just to the AdS boundary. In this case, we can conjecture that the dual CFT state does not arise from a partial trace over a pure state involving a dS boundary.

ACKNOWLEDGMENTS

We thank S. Baiguera for useful discussions and comments on the draft. The work of N. Z. is supported by MEXT KAKENHI Grant-in-Aid for Transformative Research Areas A "Extreme Universe" No. 21H05184.

APPENDIX A: DETAILS ABOUT PENROSE DIAGRAMS

In this appendix we describe our conventions for Penrose diagrams. For the BTZ external region, the relation between the coordinates $(\tilde{t}, \tilde{r})$ of the Penrose diagram and the EF coordinates (u, v) can be expressed as

$$\tilde{t} = \frac{\pm\tan^{-1}(e^{v\sqrt{\mu}}) - \tan^{-1}(e^{-u\sqrt{\mu}})}{2},$$
$$\tilde{r} = \frac{\pm\tan^{-1}(e^{v\sqrt{\mu}}) + \tan^{-1}(e^{-u\sqrt{\mu}})}{2}, \tag{A1}$$

where the first sign is for $r > \sqrt{\mu}$ and the second sign for $r < \sqrt{\mu}$.

For the dS spacetime interior, we use the following choice of Penrose diagram coordinates

$$\tilde{t} = \frac{\tan^{-1}(e^{u\sqrt{\lambda}}) \mp \tan^{-1}(e^{-v\sqrt{\lambda}})}{2},$$
$$\tilde{r} = \frac{\tan^{-1}(e^{u\sqrt{\lambda}}) \pm \tan^{-1}(e^{-v\sqrt{\lambda}})}{2}, \tag{A2}$$

where the first sign is for $r < 1/\sqrt{\lambda}$ and the second sign for $r > 1/\sqrt{\lambda}$.

In this paper, Penrose diagrams are obtained by a parametric plot of the coordinates $(\pm\tilde{r}, \pm\tilde{t})$, using Eq. (A1) for the external BTZ region and Eq. (A2) for the dS interior. The direction of increasing t on each side of the diagrams is shown in Fig. 6.

APPENDIX B: DERIVATION OF THE REFRACTION LAW FOR EXTREMAL SURFACES

Let us assume that the change of variable between $t_{i,o}$ is of the form

$$t_o = G(r) t_i. \tag{B1}$$

The function G will be specified later by requiring the proper time on the bubble to be continuous. In terms of the interior time coordinate t_i, the outside metric in Eq. (2.1) reads

$$ds_o^2 = -f_o G^2 dt_i^2 - f_o \frac{d(G^2)}{dr} t_i dr dt_i + \frac{1 - f_o^2 \left(\frac{dG}{dr}\right)^2 t_i^2}{f_o} dr^2 + r^2 d\theta^2, \tag{B2}$$

where f_i and f_o are functions of r given in Eqs. (2.2) and (2.3). Hence, both the interior and the exterior metrics have the following form:

$$ds^2 = -g(r, t_i) dt_i^2 + \frac{dr^2}{f(r, t_i)} + 2h(r, t_i) dr dt_i + r^2 d\theta^2, \tag{B3}$$

where for the interior metric

$$g(r, t_i) = f_i, \qquad f(r, t_i) = f_i, \qquad h(r, t_i) = 0, \tag{B4}$$

while for the exterior metric

$$g(r, t_i) = G^2 f_o,$$
$$f(r, t_i) = \frac{f_o}{1 - f_o^2 (\frac{dG}{dr})^2 t_i^2},$$
$$h(r, t_i) = -f_o G \frac{dG}{dr} t_i. \tag{B5}$$

For later purposes, it is useful to evaluate the following quantities both inside and outside the bubble:

$$\left.\frac{g + fh^2}{f}\right|_i = 1, \qquad \left.\frac{g + fh^2}{f}\right|_o = G^2. \tag{B6}$$

For the metric in Eq. (B3), the volume functional is

$$\mathcal{L} = r\sqrt{-g(r,t_i)t_i'^2 + \frac{r'^2}{f(r,t_i)} + 2h(r,t_i)r't_i'}$$
$$\mathcal{V}_{i,o} = 2\pi\int \mathcal{L}dl,. \tag{B7}$$

It is convenient to fix the gauge as in Eq. (3.6), which is equivalent to

$$\sqrt{-g(r,t_i)t_i'^2 + \frac{r'^2}{f(r,t_i)} + 2h(r,t_i)r't_i'} = r. \tag{B8}$$

1. Static bubble

At constant r, continuity of the proper time on the domain wall fixes

$$G(r) = \pm\sqrt{\frac{f_i(r)}{f_o(r)}}. \tag{B9}$$

Let us discuss the extremal codimension-one surfaces. In this case, the functions f, g, h do not depend on t_i, so there is a conserved quantity

$$\hat{P} = \frac{\partial\mathcal{L}}{\partial t_i'} = \frac{-gt_i' + hr'}{\sqrt{-g(r,t_i)t_i'^2 + \frac{r'^2}{f(r,t_i)} + 2h(r,t_i)r't_i'}}r. \tag{B10}$$

With our gauge choice, the conserved quantity can be written as

$$\hat{P}^2 = \left(\frac{g+fh^2}{f}\right)(r')^2 - gr^2. \tag{B11}$$

Using Eqs. (B6) and (B9), together with the fact that g is continuous on the bubble, we find

$$(r_i')^2 = \frac{f_i}{f_o}(r_o')^2. \tag{B12}$$

From Eq. (2.27), we finally get

$$P_o^2 = \frac{f_o(R)}{f_i(R)}P_i^2 = \mu_0^2 P_i^2. \tag{B13}$$

2. Dynamical bubble

For dynamical bubbles, the functions f, g, h depend on t_i. All the derivatives

$$\partial_{t_i}f, \qquad \partial_{t_i}h, \qquad \partial_r f, \qquad \partial_r h,$$

will have a Dirac delta contribution localized on the surface of the bubble

$$t_i = T_i(\tau), \qquad r = R(\tau).$$

We impose the condition that this delta function contribution is constant on the surface of the bubble:

$$\left.\frac{df(r,t_i)}{d\tau}\right|_{\text{bubble}} = \frac{df(R(\tau),T_i(\tau))}{d\tau} = \dot{T}_i\partial_{t_i}f + \dot{R}\partial_r f = 0, \tag{B14}$$

which implies

$$\partial_{t_i}f = -\frac{dR}{dT_i}\partial_r f. \tag{B15}$$

So we expect

$$\partial_r f = \frac{1}{\sqrt{1+\left(\frac{dR}{dT_i}\right)^2}}\delta(r-R(\tau))\Delta f,$$
$$\partial_{t_i}f = -\frac{dR}{dT_i}\frac{1}{\sqrt{1+\left(\frac{dR}{dT_i}\right)^2}}\delta(r-R(\tau))\Delta f,$$

where Δf is the discontinuity of f on the surface of the bubble. An analogous equation holds for h.

Let us introduce the variables s and w such that

$$\begin{pmatrix} t_i \\ r \end{pmatrix} = \begin{pmatrix} \cos\psi & -\sin\psi \\ \sin\psi & \cos\psi \end{pmatrix}\begin{pmatrix} s \\ w \end{pmatrix}, \tag{B16}$$

where

$$\sin\psi = \frac{\dot{R}}{\sqrt{\dot{R}^2+\dot{T}_i^2}}, \qquad \cos\psi = \frac{\dot{T}_i}{\sqrt{\dot{R}^2+\dot{T}_i^2}},$$
$$\tan\psi = \frac{dR}{dT_i}. \tag{B17}$$

The derivative of f with respect to s is

$$\frac{\partial f}{\partial s} = \frac{\partial t_i}{\partial s}\partial_{t_i}f + \frac{\partial r}{\partial s}\partial_r f = \frac{\dot{T}_i\partial_{t_i}f + \dot{R}\partial_r f}{\sqrt{\dot{R}^2+\dot{T}_i{}^2}}. \tag{B18}$$

A similar property is valid for h. From Eq. (B15), we thus find that the relations $\partial_s f = 0$ and $\partial_s h = 0$ are satisfied by the Dirac delta term.

Going back to the volume functional in Eq. (B7), we can express it in the (s,w) coordinates. In the approximation in which we consider just the "fast" dependence of the Lagrangian due to discontinuities at the two sides of the

domain wall, the Lagrangian density is independent of s. We have then a conserved quantity of the form

$$\hat{P} = \frac{\partial \mathcal{L}}{\partial s'} = (hr' - gt_i')\cos\psi + \left(\frac{r'}{f} + ht_i'\right)\sin\psi. \tag{B19}$$

The quantity $\hat{P}$ is not globally conserved on the codimension-one extremal surface, but just before and after the collision with the Dirac delta domain wall. Plugging the gauge fixing condition (B8) in, we get

$$\hat{P}^2 = \left(\frac{g+fh^2}{fg} r' \sin\psi \pm \frac{(g\cos\psi - h\sin\psi)}{g} \times \sqrt{\frac{g+fh^2}{f}(r')^2 - gr^2}\right)^2. \tag{B20}$$

The conserved quantities inside and outside the domain wall are

$$\hat{P}_i^2 = \left(\frac{\sin\psi}{f_i} r_i' \pm \sqrt{(r_i')^2 - f_i r^2}\cos\psi\right)^2,$$
$$\hat{P}_o^2 = \left(\frac{1}{f_o} r_o' \sin\psi \pm \left(G\cos\psi + \frac{dG}{dr} t_i \sin\psi\right) \sqrt{(r_o')^2 - f_o r^2}\right)^2. \tag{B21}$$

Combining the condition $\hat{P}_i^2 = \hat{P}_o^2$ with Eqs. (B17) and (B1), we find

$$\left(\frac{1}{f_i} r_i' \pm \sqrt{(r_i')^2 - f_i r^2}\frac{dT_i}{dR}\right)^2 = \left(\frac{1}{f_o} r_o' \pm \frac{dT_o}{dR}\sqrt{(r_o')^2 - f_o r^2}\right)^2. \tag{B22}$$

We can consider the following crosschecks of Eq. (B22):

(i) For $\psi = 0$, it reproduces the static bubble result in Eq. (B13).

(ii) For a bubble moving at the speed of light, we have

$$\frac{dT_{i,o}}{dR} = \pm\frac{1}{f_{i,o}}. \tag{B23}$$

Specializing Eq. (B22) to Eq. (B23) and combining with Eq. (3.7), we find $V_i' = V_o'$ or $U_i' = U_o'$, depending on the choice of sign. This is in agreement with the results in [81,82].

Using the notation in Eq. (3.15), the refraction condition (B22) can be written in the covariant form

$$(g_i)_{\mu\nu}\frac{dx_i^\mu}{dl}\frac{dX_i^\nu}{d\tau} = \pm(g_o)_{\mu\nu}\frac{dx_o^\mu}{dl}\frac{dX_o^\nu}{d\tau}. \tag{B24}$$

By continuity with the case where there is no bubble into the system, the physical solution should be the one with the + sign, which we consider in Eq. (3.16).

APPENDIX C: TECHNICAL DETAILS FOR SMOOTH EXTREMAL SURFACES

1. Solution with $P_o < 0$

With the assumption of negative P_o and with the choice of sign for $\frac{dT_o}{dR}$ in Eq. (4.3), Eq. (4.2) is solved by

$$P_o^2 = -R^4 + \mu R^2 + \frac{((\mu+1)^2 + R^4(\kappa^2(\lambda-1)+(\lambda+1)^2) + R^2(\kappa^2(\mu-1) - 2(\lambda+1)(\mu+1)))^2}{4\kappa^4 R^2(1-\lambda R^2)}.$$
$$\rho_o = -\frac{R^4(\kappa^2(\lambda-1)+(\lambda+1)^2) - R^2(2(\lambda+1)(\mu+1) - \kappa^2(\mu-1)) + (\mu+1)^2}{2\kappa^2 R\sqrt{1-\lambda R^2}}, \tag{C1}$$

A direct calculation gives that $\rho_o(R_{\max})$ in Eq. (C1) is the opposite of $\rho_o(R_{\max})$ in Eq. (4.4). The same holds true for $\rho_o(R_{\min})$. So, the solution in Eq. (C1) corresponds to a "reflection" of the codimension-one extremal surface, and as such should be discarded. Note that both the solutions in Eqs. (4.5) and (C1) vanish for $r = R_{\max} = R_{\min}$.

2. Sign of $\rho_o(R)$ for small bubbles

The function $\rho_o(R)$ in Eq. (4.4) vanishes for $R = R_0$, where

$$R_0(\mu) = \sqrt{\frac{1-\mu}{\kappa^2+\lambda-1}}. \tag{C2}$$

Therefore, if either $R_0(\mu)$ is not a real number or $R_0 > R_{\max}$, the sign of $\rho_o(R)$ does not change along the surface of the bubble. Conversely, if $R_0(\mu)$ is real and $R_0 < R_{\max}$, $\rho_o(R)$ changes sign along the bubble. With a direct calculation, it can be checked that

$$R_0(\mu_s) = \sqrt{\mu_s} = R_{\max}(\mu_s). \tag{C3}$$

There are then four possible behaviors of $\rho_o(R)$ on the domain wall:

(A) $\mu < \mu_s$ and $\lambda + \kappa^2 > 1$. The function $\rho_o(R)$ is always positive.
(B) $\mu < \mu_s$ and $\lambda + \kappa^2 < 1$. When R_0 is real, $\rho_o(R)$ is positive for $R_0 < R \leq R_{\max}$ and negative for $0 < R < R_0$. When R_0 is imaginary, $\rho_o(R)$ is always positive.
(C) $\mu > \mu_s$ and $\lambda + \kappa^2 > 1$. When R_0 is real, $\rho_o(R)$ is negative for $R_0 < R \leq R_{\max}$ and positive for $0 < R < R_0$. When R_0 is imaginary, $\rho_o(R)$ is always negative.
(D) $\mu > \mu_s$ and $\lambda + \kappa^2 < 1$. The function $\rho_o(R)$ is always negative.

With reference to Sec. IV A 2, from these considerations we find that the region of parameter space in bullet (A) belongs to case 2, while the part of parameter space in bullet (D) belongs to case 1.

3. Behavior of the complexity rate for $t_b = 0$

In this appendix, we determine the explicit value of the quantity K defined in Eq. (4.16). Let us first consider very small bubbles. Since for $t_b \to 0$ we have $\rho_o(R) > 0$, we should use Eq. (4.10) to compute $\frac{dt_b}{dP_o}$. By symmetry, $t_b = 0$ corresponds to $P_o = 0$, so

$$K = \left.\frac{dt_b}{dP_o}\right|_{P_o=0} = H - \int_{R_{\max}}^{\Lambda} \frac{1}{r(f_o(r))^{3/2}}\, dr, \tag{C4}$$

where

$$H = \left.\frac{dT_o}{dR}\frac{dR}{dP_o}\right|_{R=R_{\max}} = \frac{a}{b} \tag{C5}$$

and

$$\begin{aligned} a &= 2\sqrt{1-\lambda R_{\max}^2}(1+\mu-R_{\max}^2(1+\lambda+\kappa^2)), \\ b &= R_{\max}^2(R_{\min}^2-R_{\max}^2)(R_{\max}^2-\mu) \\ &\quad \times (\lambda+(\kappa-1)^2)(\lambda+(\kappa+1)^2). \end{aligned} \tag{C6}$$

We can use the explicit integral

$$\begin{aligned} F(r) &= \int \frac{-1}{r(r^2-\mu)^{3/2}}\, dr \\ &= \frac{1}{\mu\sqrt{r^2-\mu}} - \frac{2}{\mu^{3/2}} \tan^{-1}\sqrt{\frac{r+\sqrt{\mu}}{r-\sqrt{\mu}}} \end{aligned} \tag{C7}$$

to obtain

$$K = H - \frac{\pi}{2\mu^{3/2}} - F(R_{\max}). \tag{C8}$$

In the case of not so small bubbles, for $t_b \to 0$ we have $\rho_o(R) < 0$, so $\frac{dt_b}{dP_o}$ is given by Eq. (4.14). To perform the computation, we first send $r_{t,\mathrm{AdS}} \to r_{t,\mathrm{AdS}} + \delta$, then we use the Leibniz integral rule:

$$\begin{aligned} K = H &- \int_{r_{t,\mathrm{AdS}}+\delta}^{\Lambda} \frac{r^2}{(P_o^2 + f_o(r)r^2)^{3/2}}\, dr \\ &- \int_{r_{t,\mathrm{AdS}}+\delta}^{R} \frac{r^2}{(P_o^2 + f_o(r)r^2)^{3/2}}\, dr \\ &+ \frac{1}{\sqrt{P_o^2 + (r_{t,\mathrm{AdS}}+\delta)^2 f_o(r_{t,\mathrm{AdS}}+\delta)}} \\ &\times 2\frac{dr_{t,\mathrm{AdS}}}{dP_o}\frac{P_o}{f_o(r_{t,\mathrm{AdS}})}. \end{aligned} \tag{C9}$$

At small P_o, the following approximations are valid:

$$\begin{aligned} P_o^2 + f_o(r)r^2 &\approx (r - r_{t,\mathrm{AdS}})(r+\sqrt{\mu})r^2, \\ r_{t,\mathrm{AdS}} &\approx \sqrt{\mu} - \frac{P_o^2}{2\mu^{3/2}} + O(P_o^4), \\ \frac{dr_{t,\mathrm{AdS}}}{dP_o} &\approx -\frac{P_o}{\mu^{3/2}}, \\ \frac{1}{f_o(r_{t,\mathrm{AdS}})} &\approx -\frac{\mu}{P_o^2} + O(P_o^0). \end{aligned} \tag{C10}$$

Hence, we get

$$\begin{aligned} K = H &- \int_{r_{t,\mathrm{AdS}}+\delta}^{\Lambda} \frac{1}{r[(r+\sqrt{\mu})(r-r_{t,\mathrm{AdS}})]^{3/2}}\, dr \\ &- \int_{r_{t,\mathrm{AdS}}+\delta}^{R_{\max}} \frac{1}{r[(r+\sqrt{\mu})(r-r_{t,\mathrm{AdS}})]^{3/2}}\, dr + \frac{\sqrt{2}}{\mu^{5/4}}\frac{1}{\sqrt{\delta}} \\ &= H + F(R_{\max}) + \frac{3\pi}{2\mu^{3/2}}. \end{aligned} \tag{C11}$$

Consistently, Eqs. (C8) and (C11) matches for $\mu = \mu_s$.

In the case of large bubbles, similar calculations give

$$K = \tilde{H} + F(R_{\min}) + \frac{3\pi}{2\mu^{3/2}}, \tag{C12}$$

where

$$\tilde{H} = \left.\frac{dT_o}{dR}\frac{dR}{dP_o}\right|_{R=R_{\min}} = \frac{\tilde{a}}{\tilde{b}} \tag{C13}$$

and

$$\tilde{a} = -2\sqrt{1-\lambda R_{\rm min}^2}(1+\mu-R_{\rm min}^2(1+\lambda+\kappa^2))$$
$$\tilde{b} = R_{\rm min}^2(R_{\rm min}^2-R_{\rm max}^2)(R_{\rm min}^2-\mu) \times(\lambda+(\kappa-1)^2)(\lambda+(\kappa+1)^2). \quad \text{(C14)}$$

Note that K in Eq. (C12) is always positive, because both $F(r)+\frac{3\pi}{2\mu^{3/2}}>0$ and $\tilde{H}>0$. The latter property follows from

$$w_o(R_{\rm min})<0, \quad \text{(C15)}$$

where w_o is defined in Eq. (4.3). The inequality (C15) arises from the negativity of $w_o(R_{\rm min})$ at $\mu=0$. Indeed, no real solutions for μ to the equation $w_o(R_{\rm min})=0$ exist. Consequently, $w_o(R_{\rm min})$ never changes sign as a function of μ.

[1] J. M. Maldacena, The large N limit of superconformal field theories and supergravity, Adv. Theor. Math. Phys. **2**, 231 (1998).
[2] A. Strominger, The dS/CFT correspondence, J. High Energy Phys. 10 (2001) 034.
[3] R. Bousso, A. Maloney, and A. Strominger, Conformal vacua and entropy in de Sitter space, Phys. Rev. D **65**, 104039 (2002).
[4] V. Balasubramanian, J. de Boer, and D. Minic, Notes on de Sitter space and holography, Classical Quantum Gravity **19**, 5655 (2002).
[5] D. Anninos, T. Hartman, and A. Strominger, Higher spin realization of the dS/CFT correspondence, Classical Quantum Gravity **34**, 015009 (2017).
[6] Y. Hikida, T. Nishioka, T. Takayanagi, and Y. Taki, Holography in de Sitter Space via Chern-Simons Gauge Theory, Phys. Rev. Lett. **129**, 041601 (2022).
[7] Y. Hikida, T. Nishioka, T. Takayanagi, and Y. Taki, CFT duals of three-dimensional de Sitter gravity, J. High Energy Phys. 05 (2022) 129.
[8] G. W. Gibbons and S. W. Hawking, Cosmological event horizons, thermodynamics, and particle creation, Phys. Rev. D **15**, 2738 (1977).
[9] R. Bousso, Positive vacuum energy and the N bound, J. High Energy Phys. 11 (2000) 038.
[10] R. Bousso, Bekenstein bounds in de Sitter and flat space, J. High Energy Phys. 04 (2001) 035.
[11] V. Chandrasekaran, R. Longo, G. Penington, and E. Witten, An algebra of observables for de Sitter space, J. High Energy Phys. 02 (2023) 082.
[12] K. Maeda, T. Koike, M. Narita, and A. Ishibashi, Upper bound for entropy in asymptotically de Sitter space-time, Phys. Rev. D **57**, 3503 (1998).
[13] T. Banks, Some thoughts on the quantum theory of de Sitter space, arXiv:astro-ph/0305037.
[14] N. Goheer, M. Kleban, and L. Susskind, The trouble with de Sitter space, J. High Energy Phys. 07 (2003) 056.
[15] M. K. Parikh and E. P. Verlinde, De Sitter holography with a finite number of states, J. High Energy Phys. 01 (2005) 054.
[16] T. Banks, B. Fiol, and A. Morisse, Towards a quantum theory of de Sitter space, J. High Energy Phys. 12 (2006) 004.
[17] D. Anninos, S. A. Hartnoll, and D. M. Hofman, Static patch solipsism: Conformal symmetry of the de Sitter worldline, Classical Quantum Gravity **29**, 075002 (2012).
[18] L. Susskind, De Sitter holography: Fluctuations, anomalous symmetry, and wormholes, Universe **7**, 464 (2021).
[19] F. Sanches and S. J. Weinberg, Holographic entanglement entropy conjecture for general spacetimes, Phys. Rev. D **94**, 084034 (2016).
[20] Y. Nomura, P. Rath, and N. Salzetta, Spacetime from unentanglement, Phys. Rev. D **97**, 106010 (2018).
[21] Y. Nomura, Spacetime and universal soft modes—black holes and beyond, Phys. Rev. D **101**, 066024 (2020).
[22] S. Ryu and T. Takayanagi, Holographic Derivation of Entanglement Entropy from AdS/CFT, Phys. Rev. Lett. **96**, 181602 (2006).
[23] V. E. Hubeny, M. Rangamani, and T. Takayanagi, A covariant holographic entanglement entropy proposal, J. High Energy Phys. 07 (2007) 062.
[24] L. Susskind, Entanglement and chaos in de Sitter space holography: An SYK example, J. Hologr. Appl. Phys. **1**, 1 (2021).
[25] E. Shaghoulian, The central dogma and cosmological horizons, J. High Energy Phys. 01 (2022) 132.
[26] E. Shaghoulian and L. Susskind, Entanglement in de Sitter space, J. High Energy Phys. 08 (2022) 198.
[27] L. Susskind, Black holes hint towards de Sitter-matrix theory, arXiv:2109.01322.
[28] L. Susskind, Scrambling in double-scaled SYK and de Sitter space, arXiv:2205.00315.
[29] H. Lin and L. Susskind, Infinite temperature's not so hot, arXiv:2206.01083.
[30] C. Murdia, Y. Nomura, and K. Ritchie, Black hole and de Sitter microstructures from a semiclassical perspective, Phys. Rev. D **107**, 026016 (2023).
[31] L. Susskind, De Sitter space, double-scaled SYK, and the separation of scales in the semiclassical limit, arXiv:2209.09999.
[32] A. A. Rahman, dS JT gravity and double-scaled SYK, arXiv:2209.09997.
[33] B. Bhattacharjee, P. Nandy, and T. Pathak, Krylov complexity in large-q and double-scaled SYK model, arXiv:2210.02474.

[34] L. Susskind, Entanglement is not enough, Fortschr. Phys. **64**, 49 (2016).
[35] L. Susskind, *Three Lectures on Complexity and Black Holes* (Springer, New York, 2020), ISBN 978-3-030-45108-0, 978-3-030-45109-7, 10.1007/978-3-030-45109-7.
[36] S. Chapman and G. Policastro, Quantum computational complexity from quantum information to black holes and back, Eur. Phys. J. C **82**, 128 (2022).
[37] T. Hartman and J. Maldacena, Time evolution of entanglement entropy from black hole interiors, J. High Energy Phys. 05 (2013) 014.
[38] L. Susskind, Computational complexity and black hole horizons, Fortschr. Phys. **64**, 24 (2016); **64**, 44(A) (2016).
[39] S. Aaronson, The complexity of quantum states and transformations: From quantum money to black holes, arXiv: 1607.05256.
[40] Michael A. Nielsen, A geometric approach to quantum circuit lower bounds, Quantum Inf. Comput. **6**, 213 (2006).
[41] A. R. Brown, M. H. Freedman, H. W. Lin, and L. Susskind, Effective geometry, complexity, and universality, arXiv:2111.12700.
[42] Mark R. Dowling and Michael A. Nielsen, The geometry of quantum computation, Quantum Inf. Comput. **8**, 861 (2010).
[43] A. R. Brown, L. Susskind, and Y. Zhao, Quantum complexity and negative curvature, Phys. Rev. D **95**, 045010 (2017).
[44] A. R. Brown and L. Susskind, Complexity geometry of a single qubit, Phys. Rev. D **100**, 046020 (2019).
[45] R. Auzzi, S. Baiguera, G. B. De Luca, A. Legramandi, G. Nardelli, and N. Zenoni, Geometry of quantum complexity, Phys. Rev. D **103**, 106021 (2021).
[46] A. R. Brown, A quantum complexity lowerbound from differential geometry, Nat. Phys. **19**, 401 (2023).
[47] P. Basteiro, J. Erdmenger, P. Fries, F. Goth, I. Matthaiakakis, and R. Meyer, Quantum complexity as hydrodynamics, Phys. Rev. D **106**, 065016 (2022).
[48] R. Jefferson and R. C. Myers, Circuit complexity in quantum field theory, J. High Energy Phys. 10 (2017) 107.
[49] S. Chapman, M. P. Heller, H. Marrochio, and F. Pastawski, Toward a Definition of Complexity for Quantum Field Theory States, Phys. Rev. Lett. **120**, 121602 (2018).
[50] P. Caputa, N. Kundu, M. Miyaji, T. Takayanagi, and K. Watanabe, Anti-de Sitter Space from Optimization of Path Integrals in Conformal Field Theories, Phys. Rev. Lett. **119**, 071602 (2017).
[51] P. Caputa and J. M. Magan, Quantum Computation as Gravity, Phys. Rev. Lett. **122**, 231302 (2019).
[52] J. Erdmenger, M. Gerbershagen, and A. L. Weigel, Complexity measures from geometric actions on Virasoro and Kac-Moody orbits, J. High Energy Phys. 11 (2020) 003.
[53] M. Flory and M. P. Heller, Geometry of complexity in conformal field theory, Phys. Rev. Res. **2**, 043438 (2020).
[54] N. Chagnet, S. Chapman, J. de Boer, and C. Zukowski, Complexity for Conformal Field Theories in General Dimensions, Phys. Rev. Lett. **128**, 051601 (2022).
[55] D. Stanford and L. Susskind, Complexity and shock wave geometries, Phys. Rev. D **90**, 126007 (2014).
[56] A. R. Brown, D. A. Roberts, L. Susskind, B. Swingle, and Y. Zhao, Holographic Complexity Equals Bulk Action?, Phys. Rev. Lett. **116**, 191301 (2016).
[57] A. R. Brown, D. A. Roberts, L. Susskind, B. Swingle, and Y. Zhao, Complexity, action, and black holes, Phys. Rev. D **93**, 086006 (2016).
[58] J. Couch, W. Fischler, and P. H. Nguyen, Noether charge, black hole volume, and complexity, J. High Energy Phys. 03 (2017) 119.
[59] A. Belin, R. C. Myers, S. M. Ruan, G. Sárosi, and A. J. Speranza, Does Complexity Equal Anything?, Phys. Rev. Lett. **128**, 081602 (2022).
[60] A. Belin, R. C. Myers, S. M. Ruan, G. Sárosi, and A. J. Speranza, Complexity equals anything II, J. High Energy Phys. 01 (2023) 154.
[61] F. Omidi, Generalized volume-complexity for two-sided hyperscaling violating black branes, J. High Energy Phys. 01 (2023) 105.
[62] L. Susskind, The typical-state paradox: Diagnosing horizons with complexity, Fortschr. Phys. **64**, 84 (2016).
[63] E. Jorstad, R. C. Myers, and S. M. Ruan, Holographic complexity in dS_{d+1}, J. High Energy Phys. 05 (2022) 119.
[64] D. Anninos and D. M. Hofman, Infrared realization of dS_2 in AdS_2, Classical Quantum Gravity **35**, 085003 (2018).
[65] D. Anninos, D. A. Galante, and D. M. Hofman, De Sitter horizons & holographic liquids, J. High Energy Phys. 07 (2019) 038.
[66] A. Biasi, O. Evnin, and S. Sypsas, de Sitter Bubbles from Anti–de Sitter Fluctuations, Phys. Rev. Lett. **129**, 251104 (2022).
[67] S. Chapman, D. A. Galante, and E. D. Kramer, Holographic complexity and de Sitter space, J. High Energy Phys. 02 (2022) 198.
[68] B. Freivogel, V. E. Hubeny, A. Maloney, R. C. Myers, M. Rangamani, and S. Shenker, Inflation in AdS/CFT, J. High Energy Phys. 03 (2006) 007.
[69] Z. Fu and D. Marolf, Bag-of-gold spacetimes, Euclidean wormholes, and inflation from domain walls in AdS/CFT, J. High Energy Phys. 11 (2019) 040.
[70] S. K. Blau, E. I. Guendelman, and A. H. Guth, The dynamics of false vacuum bubbles, Phys. Rev. D **35**, 1747 (1987).
[71] E. Farhi and A. H. Guth, An obstacle to creating a universe in the laboratory, Phys. Lett. B **183**, 149 (1987).
[72] E. Farhi, A. H. Guth, and J. Guven, Is it possible to create a universe in the laboratory by quantum tunneling?, Nucl. Phys. **B339**, 417 (1990).
[73] M. Banados, C. Teitelboim, and J. Zanelli, The Black Hole in Three-Dimensional Space-Time, Phys. Rev. Lett. **69**, 1849 (1992).
[74] J. M. Maldacena, Eternal black holes in anti-de Sitter, J. High Energy Phys. 04 (2003) 021.
[75] W. Israel, Singular hypersurfaces and thin shells in general relativity, Nuovo Cimento B **44S10**, 1 (1966); **48**, 463(E) (1967).
[76] E. Poisson, *A Relativist's Toolkit: The Mathematics of Black-Hole Mechanics* (Cambridge University Press, Cambridge, England, 2009), 10.1017/CBO9780511606601.
[77] D. Marolf, Black holes, AdS, and CFTs, Gen. Relativ. Gravit. **41**, 903 (2009).
[78] T. Jacobson, On the nature of black hole entropy, AIP Conf. Proc. **493**, 85 (1999).

[79] P. Iglesias-Zemmour, Refraction and reflexion according to the principle of general covariance, J. Geom. Phys. **142**, 1 (2019).
[80] V. Balasubramanian, A. Bernamonti, J. de Boer, N. Copland, B. Craps, E. Keski-Vakkuri, B. Muller, A. Schafer, M. Shigemori, and W. Staessens, Holographic thermalization, Phys. Rev. D **84**, 026010 (2011).
[81] S. Chapman, H. Marrochio, and R. C. Myers, Holographic complexity in Vaidya spacetimes. Part I, J. High Energy Phys. 06 (2018) 046.
[82] S. Chapman, H. Marrochio, and R. C. Myers, Holographic complexity in Vaidya spacetimes. Part II, J. High Energy Phys. 06 (2018) 114.
[83] D. Carmi, S. Chapman, H. Marrochio, R. C. Myers, and S. Sugishita, On the time dependence of holographic complexity, J. High Energy Phys. 11 (2017) 188.
[84] S. Lloyd, Ultimate physical limits to computation, Nature (London) **406**, 1047 (2000).
[85] J. Couch, S. Eccles, W. Fischler, and M. L. Xiao, Holographic complexity and noncommutative gauge theory, J. High Energy Phys. 03 (2018) 108.
[86] B. Swingle and Y. Wang, Holographic complexity of Einstein-Maxwell-dilaton gravity, J. High Energy Phys. 09 (2018) 106.
[87] R. Q. Yang, C. Niu, C. Y. Zhang, and K. Y. Kim, Comparison of holographic and field theoretic complexities for time dependent thermofield double states, J. High Energy Phys. 02 (2018) 082.
[88] S. Mahapatra and P. Roy, On the time dependence of holographic complexity in a dynamical Einstein-dilaton model, J. High Energy Phys. 11 (2018) 138.
[89] A. Bernamonti, F. Bigazzi, D. Billo, L. Faggi, and F. Galli, Holographic and QFT complexity with angular momentum, J. High Energy Phys. 11 (2021) 037.
[90] R. Q. Yang, H. S. Jeong, C. Niu, and K. Y. Kim, Complexity of holographic superconductors, J. High Energy Phys. 04 (2019) 146.
[91] R. Auzzi, S. Bolognesi, E. Rabinovici, F. I. Schaposnik Massolo, and G. Tallarita, On the time dependence of holographic complexity for charged AdS black holes with scalar hair, J. High Energy Phys. 08 (2022) 235.
[92] S. Chapman, H. Marrochio, and R. C. Myers, Complexity of formation in holography, J. High Energy Phys. 01 (2017) 062.
[93] M. Alishahiha, Holographic complexity, Phys. Rev. D **92**, 126009 (2015).
[94] D. Carmi, R. C. Myers, and P. Rath, Comments on holographic complexity, J. High Energy Phys. 03 (2017) 118.
[95] C. A. Agón, M. Headrick, and B. Swingle, Subsystem complexity and holography, J. High Energy Phys. 02 (2019) 145.